Title: Spatial mapping of dextran sodium sulphate-induced intestinal inflammation and its systemic effects

Authors: Lauren Adams[1], Orhan Rasid[1], Heather Hulme[2], Tezz Quon[1], Richard Burchmore[1], Simon Milling[1], Richard Goodwin[1,2], Daniel M. Wall[1]

[1]School of Infection and Immunology, College of Medical, Veterinary and Life Sciences, Sir Graeme Davies Building, University of Glasgow, Glasgow G12 8TA, United Kingdom.
[2]Imaging and Data Analytics, Clinical Pharmacology and Safety Sciences, Biopharmaceuticals R&D, AstraZeneca, Cambridge CB4 0WG, U.K.

Corresponding author email address: Donal.Wall@glasgow.ac.uk;

Abstract:
Inflammatory bowel disease (IBD) is a multifactorial disease and patients frequently experience extraintestinal manifestations affecting multiple sites. Causes of systemic inflammation remain poorly understood but molecules originating from the intestine likely play a role with microbial and host small molecules polarizing host immune cells towards a pro- or anti-inflammatory phenotype. Using the dextran sodium sulphate (DSS) mouse model, which mimics models the disrupted barrier function in IBD, microbial dysbiosis and immune cell dysregulation in IBD, we investigated metabolomic and phenotypic changes at intestinal and systemic sites. Through mass spectrometry imaging we mapped the spatial distribution and relative abundance of molecules and cell types across a range of tissues during colitis. This approach revealed specific molecular changes across a range of organs including the colon, ileum, liver, spleen and kidney, while no molecular changes were observed in the lungs of DSS-treated mice. Specific molecules, identified as contributing to the statistical separation of treated from control mice, were then spatially localized within organs to determine their effects on cellular phenotypes through imaging mass cytometry. Additionally, molecules that were significantly changed across multiple systemic sites in response to inflammation were identified. This spatial approach identified drivers of inflammation both locally in the intestine and systemically and has highlighted a number of molecules not previously implicated in inflammation linked to IBD or the systemic effects of intestinal inflammation. Together this data shows that gaining a better understanding of metabolic pathways and identifying molecular disease biomarkers within the intestine and systemic organs during IBD, might improve our understanding of disease aetiology and aid the development of new targeted therapies.

Introduction:

Inflammatory bowel diseases (IBD) including Crohn's Disease (CD) are complex multifactorial diseases characterised by chronic relapsing-remitting inflammation. Many IBD patients experience extraintestinal manifestations (EIM) of disease that can affect nearly any organ system including dermatological, hepatopancreatobiliary, ocular, renal, neural and pulmonary systems (1). Complications such as non-alcoholic fatty liver disease (NAFLD) and gallstones have also been associated with disease and linked to metabolic dysfunction (2). The understanding of the inflammatory processes that underpin IBD onset and progression have been advanced due to the development of numerous murine models of intestinal colitis. These *in vivo* models have enabled characterisation of the complexity of IBD pathogenesis by reflecting underlying molecular mechanisms of IBD such as genetic mutations, impaired barrier function, and dysfunctional innate and adaptive immune responses. Experimental models, such as the most common chemically induced colitis model using dextran sodium sulphate (DSS), are quick, reproducible, and controllable (3). DSS is a sulphate polysaccharide that acts as a colitogen *in vivo* with anticoagulant properties inducing similar clinical symptoms and histological features to those of human IBD. Colitis with DSS develops within one week and severity can be measured by weight loss, rectal bleeding, stool consistency and colonic shortening. This model, in a similar manner to human disease, also exhibits EIMs including impaired brain function, inflammation of the liver and lungs, splenomegaly and immune cell dysfunction in the spleen, as well as metabolic changes in the kidney (4, 5).

DSS-induced acute inflammation mostly affects, but is not limited to, the colonic mucosa as the negatively charged sulphate groups are thought to damage the intestinal mucosa and epithelial monolayer lining (6). The damage to the epithelial cells involves loss of crypts and an altered immune response characterised by infiltration of granulocytes (7). Damage to epithelial cells leads to increasing gut permeability, allowing commensal gut microorganisms to penetrate through the dysfunctional epithelial tight junctions into the lamina propria (6, 7). This influx of microbiota in IBD can result in the activation of intestinal macrophages which secrete high levels of inflammatory cytokines such as tumour necrosis factor alpha (TNF-α), interleukin-1 beta (IL-1β), and interleukin-6 (IL-6) (8). These cytokines act as chemoattractants to recruit immune cells such as dendritic cells, T cells, B cells and neutrophils into the colon which perpetuates the inflammatory environment (9). DSS-induced colitis has highlighted that intestinal bacteria are essential for the development of inflammation that is representative of human IBD (7, 10). Studies using germ-free (GF) mice showed that DSS induced only minimal inflammation, represented by no colonic thickening or shortening and low levels of proinflammatory cytokines, in spite of mice having impaired barrier function (10). Conventionally colonized mice, treated with antibiotics to perturb the

intestinal microbiota, had an increased inflammatory response but were less prone to epithelial injury. This was attributed to an increase in interleukin-10 (IL-10) and increases in other barrier preservation related markers (10). Furthermore, longitudinal microbiome analysis studies have indicated that DSS-induced colitis results in dynamic fluctuations in microbial diversity, transitioning from a normal state to dysbiosis (11). Whether gut microbial dysbiosis is a cause or a consequence of DSS induced colitis has yet to be fully elucidated and warrants further investigation, however the evidence suggests that DSS-induced colitis involves the simultaneous interactions between the epithelial barrier, intestinal microbiota, and the host immune response (11).

Bacterial metabolites can act as signals that affect immune homeostasis, host energy metabolism and the maintenance of mucosal integrity (12). Studies have found that microbial metabolites such as ursodeoxycholic acid and its derivatives can reduce the severity of DSS-induced colitis by inhibiting the expression of proinflammatory mucosal cytokines and apoptosis of epithelial cells (13, 14). Furthermore, tryptophan can be metabolised by intestinal bacteria into a series of indole-metabolites such as indole-3-propionic acid which has been shown to reduce intestinal permeability and protect mice from DSS-induced colitis (15). Therefore, intestinal microbial dysbiosis during DSS colitis may result in the downregulation of specific metabolites involved in immune regulation; thus, promoting inflammatory processes (12, 13, 15). Multi-omic approaches have been implemented to gain a better understanding of the molecular basis of IBD pathogenesis (16). Studies have found that DSS induced colitis significantly alters the metabolome and pathways such as amino acid and lipid metabolism are upregulated as severity of inflammation increases (17). The activation of proinflammatory responses in the DSS colitis model also involves altered host metabolites as partial least squares-discriminant analysis (PLS-DA) metabolomic analysis has shown that succinic acid, glutamic acid, and glutamine are the main differentiators between colitis groups and controls (18). Therefore, gaining a better understanding of the bacterial and host metabolites that interact with immune cells during DSS-induced colitis can aid in identifying mechanisms of pathology.

Here we used the DSS colitis model to study the effect microbial and host metabolites play in disease. Using mass spectrometry imaging and multivariate analysis we identified molecular changes in the colon and ileum during DSS induced colitis that may be potential biomarkers of disease. Furthermore, we investigated the systemic metabolic changes in the liver, kidney, spleen, and lung as a result of intestinal inflammation, that may have implications for health. Imaging mass cytometry was also employed to better understand cellular changes associated with metabolic changes within the colon, ileum and liver that may be contributing to the onset or perpetuation of inflammation.

Materials and methods:

Animals and ethical approval

Male C57BL/6 mice (7-8 weeks old) were purchased from Envigo and housed in sterile cages. Mice received a standard laboratory chow diet. Approval for these procedures was given prior to their initiation by an internal University of Glasgow ethics committee and all procedures were carried out in accordance with the relevant guidelines and regulations as outlined by the U.K. Home Office (PPL P64BCA712).

Induction of colitis and evaluation of colitis clinical scores

Dextran sodium sulphate (DSS) with a molecular weight of 40 kDa was purchased from Alfa Aesar by Thermo Fisher Scientific. Following a 7-day adaptation period, mice were randomly assigned to groups (5 mice per group), consisting of a normal drinking water control or drinking water supplemented with 3% weight over volume DSS for 7 days. Mice were observed daily for clinical symptoms of colitis and body weight was monitored. Immediately before and at the end of the experiment, fresh faeces were sampled from each mouse for gut microbiota compositional analysis.

Tissue preparation

After euthanasia of mice the entire colon was removed, and length was recorded, without stretching. Colon and ileum contents were gently removed, cut longitudinally along the mesenteric line and swissed rolled before embedding into hydropropyl-methylcellulose/ polyvinylpyrrolidone hydrogel (Sigma-Aldrich). Tissue was then snap frozen in a slurry of dry ice and isopropanol (Sigma-Aldrich) then rinsed in a slurry of dry ice and isopentane (Sigma-Aldrich) for 30 seconds. Frozen blocks were then left on dry ice to allow alcohol to evaporate before storing at -80°C. Tissue types including liver, kidney, spleen, and lung were also removed, frozen and stored as described. Ten micrometre (µM) thick sections were cut from frozen tissue blocks using a cryostat microtome (Thermo Scientific). Consecutive cutting of sections was repeated until enough sections were obtained, and thaw mounted onto superfrost non-conductive microscope slides for DESI-orbitrap-MSI. All slides were dried, vacuum packed and stored at −80°C following sectioning.

Desorption electrospray ionization mass spectrometry imaging (DESI-MSI)

Vacuum sealed slides were brought to room temperature (RT) before opening and all DESI-MSI experiments were set up as follows. DESI-MSI was performed on a Thermo Scientific Q-Exactive mass spectrometer equipped with an automated Prosolia 2D DESI source. A home-built DESI sprayer assembly was used with the spray tip positioned at 1.5 mm above the sample surface and at an angle of 75°. The distance between the sprayer to mass

spectrometer inlet was 7 mm with a collection angle of 10°. The spray solvent was methanol/water (95:5 v/v), delivered at 1.5 µL/ min using a Dionex Ultimate 3000 pump (Thermo Scientific) at a spray voltage of 4.5 kV. Nitrogen was used as the nebulisation gas at a pressure of 7 bars. The Q-Exactive mass spectrometer was operated in positive ion and negative ion mode for all analysis using an S-Lens setting of 75 V. To acquire full mass spectra in the mass range of *m/z* 100–1000 a mass resolution of 70000, AGC target of 5000000 and injection time of 150 ms was used. The .raw files were converted into mzML files using ProteoWizard msConvert and compiled into. imzML format using imzML converter version 1. Data sets were then converted into .slx files and analysed using SCiLS Lab MVS (version 2020b Premium 3D). All DESI data analysis is performed on root mean square (RMS) normalised data. Relative operating characteristic (ROC) curve analysis was performed to visualize the discrimination capability of an *m/z* value between two conditions. Area under the curve (AUC) values were generated by ROC analysis and cut off ranges were set at AUC>0.75 and AUC<0.25 to produce a list of *m/z* that might discriminate between conditions.

Multivariate and univariate analysis

Following ROC analysis, unsupervised and supervised multiclass classification and correlation were performed to visualise data and highlight metabolites of interest. This multivariate analysis (MVA) was performed using SIMCA 17 software package (Sartorius Stedim Biotech). Unsupervised principal component analysis (PCA) was applied to obtain on overview of data and detect any potential outliers. Subsequently, supervised partial least squares-discriminate analysis (PLS-DA) was used to identify specific changes amongst the groups. In PLS-DA, the *Y* variable was assigned to a defined class and corresponded to *X* variable. The model was generated after the data was autofitted according to R^2, Q^2, and classification performance. The quality of the model was validated using two parameters: R2Ycum (goodness of fit) and Q2cum (goodness of prediction). A threshold of >0.5 is widely accepted as good model classification to assure reliable predictive capabilities. Group separation is presented as score plots. Variable importance in projections (VIP) was used as a readout from PLS-DA that reflects the metabolites contribution to the model. A VIP score >1 indicates a higher percent variation in the model when a metabolite is included, whereas VIP<0.5 indicates that a metabolite plays a less important role. Following multivariate analysis, univariate analysis was performed in Graphpad prism (8.4.3). The measurement data were expressed as mean relative abundance ± SD. One-way ANOVA was used for comparing more than two groups and nonparametric t-test with 5% false discovery rate (FDR) correction was used for comparing two groups. Statistical significance was

established as $p<0.05$. Metabolites with a VIP>1 and/ or a p value <0.05 were selected for further analysis.

Histological staining

After DESI-MSI, tissue sections were fixed by submerging in 4% paraformaldehyde (PFA) for 10 minutes. Sections were then stained with Mayer's haematoxylin for 1 minute, before rinsing with tap water and submerging in acid alcohol. Tissue was then stained with eosin for 20 seconds, followed by rinsing with tap water and washed 3 times with absolute ethanol. Tissue sections were then submerged in xylene for 1 minute and cover slips applied using DPX mountant. Haematoxylin and eosin stained tissue was imaged with an Aperio CS2 digital pathology scanner (Aperio Tech, Oxford, UK) at 40x and observed in ImageScope software (Aperio Tech).

Identification of metabolites

Metabolites that were significantly altered in model organs were putatively identified using the Human Metabolome Database (HMDB) based on the mass accuracy provided by DESI MSI analysis. Searches were focused to mass (M) +/- most common adducts- negative mode included M-Hydrogen (H) and M+Chlorine (Cl), positive mode included M+H, M+Potassium (K) and M+Sodium (Na). To further identify metabolites, DESI-Tandem MS (MSMS) was performed on tissue sections using Thermo Scientific Q-Exactive Orbitrap mass spectrometer. The data was acquired in either positive or negative mode with a spray voltage of 4.5kV, 70,000 resolution, maximum injection time of 1000 ms, and S-lens settings of 75 V. Precursor ion mass was set with a mass tolerance of 0.5 m/z and the mass range acquired was optimised for each analyte. Higher energy collision dissociation (HCD) with normalised collision energy (NCE) was used for fragmentation of ions during MSMS measurements ranging from 10 to 50 NCE. The identities of the ions were established based on the product ion spectra after comparing to spectra from previously published data using online platforms, HMDB and mzCloud (https://www.mzcloud.org/). Spectra of standards were also acquired using DESI-MSMS and was compared to spectra from tissue, before using *in vitro* experimentation.

Metabolite enrichment analysis

Significantly changed metabolites are shown as clustered heatmaps generated by the online MetaboAnalyst 5.0 platform (https://www.metaboanalyst.ca/). All available metabolite identities were used in MetaboAnalyst metabolite set enrichment analysis (MSEA). This tool detects major pathways that are associated with the metabolites present in the study. The applied library was the KEGG human metabolic pathways, comprising of 84 metabolite sets.

The enrichment ratio was defined as the ratio of observed hits (detected metabolite) per pathway to the count expected by chance (19). One-tailed *p* values were provided after adjusting for multiple testing, enrichment was considered significant when $p<0.05$.

Imaging mass cytometry

Tissue sections were fixed using 4% paraformaldehyde for 10 minutes at room temperature (RT). This was followed by tissue permeabilization with 1 x casein solution containing 0.1% Triton X-100 for 5 minutes at room temperature (RT). Tissue was then incubated with blocking buffer (1x casein solution) for 30 minutes at RT inside a humidifier chamber. An antibody cocktail was prepared with the appropriate dilution of antibodies (Supplementary Table 1). Tissues were the fully covered with antibody solution and incubated overnight in the humidifier chamber at 4°C. DNA Ir-Intercalator (Fluidigm) was diluted 1:400 using phosphate buffered saline (PBS) and pipetted onto tissue, followed by a 30 minute incubation at RT. Tissue was washed in PBS for 5 minutes and repeated three times after each step of the protocol. After the final PBS wash, tissue was rinsed for 30 seconds in deionised water and left to dry at room temperature. Slides were then stored at RT before imaging. Tissue was imaged using the Hyperion Imaging System (Fluidigm), rasterizing at 200Hz with an ablation energy of 5 dB. Laser was frequently tuned between imaging runs to ensure tissue was fully ablated without leaving scratches on the glass. Once acquisition was complete images were exported from MCDviewer as a 32-bit TIFF an imported into HALO image analysis platform (Indica Laboratories) for analysis. Using random forest machine learning tissue classifier module, colon and ileum were segmented into muscularis and mucosa, whilst liver and lung were analysed as whole tissue and vessels based on morphology and blood vessel cell marker, CD31. The Hiplex module was firstly used to segment the DNA intercalator from each cell with a proxy for the cytoplasm being 1 μM radius from the nucleus. Thresholds were then set to define positive cell staining for each marker. Phenotypes for cells of interest were defined using markers cited in current literature (Supplementary Table 2). Percentage positive cells and percentage positive phenotype cells were the defined within tissue regions. Statistical analysis was performed in Graphpad prism, comparisons made for the DSS treated mice used T-tests to compare treatment groups to control (naïve). Differences between DSS treated and control samples were considered significant when $p<0.05$.

Microbiome sequencing and bioinformatic analysis

Fresh faecal samples were collected from the colon of individual mice after culling and immediately stored on dry ice in sterile microfuge tubes before storing at -80°C. DNA was extracted from samples using QIAamp PowerFecal Pro DNA Kit following manufacturer's

protocol (Qiagen). Where possible, stool was collected at the beginning of the experiment and prepared as described to determine microbiome changes over time. The quantity of extracted DNAs was measured using Qubit (Thermo Fisher Scientific) before storing at -20°C. Samples were analysed by Novogene for 16S rDNA Amplicon sequencing. PCR amplification of the bacterial 16S rRNA genes V3-V4 region was performed using a forward and reverse primer that were connected to barcodes for multiplexed sequencing. PCR products with the proper size were selected by 2% agarose gel electrophoresis. Equal amounts of PCR products were pooled, end-repaired, A-tailed, and further ligated with Illumina adapters. Libraries were then sequenced on a paired-end Illumina platform to generate 250 bp paired-end raw reads. Paired-end reads were assigned to samples based on their unique barcodes and truncated by cutting of the barcode and primer sequences. Paired-end reads were merged using FLASH (V1.2.7)(20). Splicing sequences called raw tags were quality filtered under specific conditions according to Qiime (V1.7.0)(21). Tags were compared with reference database (SILVA) using UCHIME algorithm to detect chimera sequences which were subsequently removed. Novogene performed analysis and plotted results using packages in R software (Version 2.15.3).

Cell-based assays for metabolite characterization

Human intestinal epithelial HCT-8 cells were purchased from the American Type Culture Collection (ATCC) and cultured in RPMI supplemented with 10% horse serum (HS), 1% penicillin/streptomycin (P/S), 1% L-glutamine and 5 mM sodium pyruvate. Cells were incubated at 37°C, 5% CO_2 and passaged every 2-3 days up to a maximum of 30 times. HS was reduced to 3% during experimentation. HCT-8 cells were seeded at 2×10^5 in 24-well plates and treated with the appropriate metabolites (cis-4,7,10,13,16,19-docosahexaenoic acid, creatine, 1-methylnicotinamide – all Merck). All metabolites used in this study were prepared by dissolving in water, filter sterilised and diluted to the appropriate concentration in cell culture media. After treatment, cells were incubated at 37°C, 5% CO_2 for 72 hours. Supernatants and lysates were collected and stored followed by the quantification of lactate dehyrodrogenase (LDH) release, caspase-3/7 activity and cytokine secretion. LDH levels were quantified in cell supernatants using an LDH-Cytotoxicity Assay Kit following manufacturers' protocol (abcam, United Kingdom). To quantify caspase-3/7 activity, cells were lysed using 0.1% TritonX-100 and stored at -20°C. Caspase-3/7 was quantified using the Apo-ONE® Homogeneous Caspase-3/7 Assay (Promega, Fisher scientific) according to the manufacturer's protocol. Assays were read on a FluoStar Optima plate reader (BMG Biotech). The protein concentration of cell lysates was also determined using a BCA protein assay kit (Thermo Scientific) and data presented depicts caspase-3/7 activity as relative

fluorescence unit (RFU) per gram of protein. ANOVA was performed for each molecule versus the control condition (cells without treatment).

The secretion of TNF-α, IL-8, IL-6 and IL-15 was quantified in cell supernatants using a sandwich ELISA Max Deluxe Set Human (Biolegend, San Diego, CA), according to the manufacturer's protocols. The secretion of IFN-γ was also quantified in cell supernatants using a sandwich mouse IFN-γ Duo Set ELISA (DY485-05, R&D systems). Standards and samples were diluted appropriately to obtain results within the stated detection levels. Absorbance was read at 450 nm and 570 nm using Fluostar Optima plate reader and results are shown as picogram (pg) per ml. The protein concentration of the cell lysate was also determined using a BCA assay (Thermo Scientific) according to manufacturer's protocol. For each assay ANOVA was performed for each molecule versus the control condition (cells without treatment).

Splenic analysis of immune cell activation and function

Spleens were collected from C5BL/6J mice and kept in in Hanks' Balanced Salt Solution (HBSS) on ice until further processing. Spleens were mechanically dissociated, homogenised, and passed through a 70 μM cell strained undergoing 2 washes (1400 rpm/ 400 g, 4°C for 7 minutes) in MB (Phosphate buffered saline (PBS) with 0.5% foetal calf serum (FCS) and 2 mM ethylenediaminetetraacetic acid (EDTA)). Red blood cells (RBC) were lysed with 1-2 ml of RBC lysis buffer for 3-5 minutes (Thermo). Following another washing step cells were counted and cultured in 96 well round-bottom plates at a final concentration of 2.5×10^6/ml in complete RPMI (RPMI with 10% FCS, 1% L-glutamine and 1% P/S). Cultured cell suspensions were stimulated with either recombinant mouse IL-12+IL-18 to activate innate and adaptive immune effector cells (both at 5 ng/ml), IL-4 to activate humoral and adaptive immune cells (10 ng/ml) or appropriately diluted metabolites (50 μM LysoPC (18:0), creatine and DHA, and 4 μM or 0.16 μM spermidine). Cells were incubated overnight at 37°C, 5% CO_2. In the final 4 hours of culture brefeldin A and monensis (eBioscience) were added to block secretion of intracellular cytokines for detection by cytometry.

Cell culture plates were centrifuged at 1400 rpm, 4°C for 7 minutes and supernatants were stored at -20°C until further use. Live/dead stain (eBioscience Fixable Viability Dye eF506) was diluted 1:1000 in clean PBS and incubated with cells for 20 minutes at 4°C. Cells were vortexed to resuspend pellet before adding 150 μL MB to each well. Isotypes were generated by taking equal volumes of each sample from 1 condition and pooling together in spare wells.

Cells were stained with antibodies to CD69 (clone H1.2F3, Biolegend), CD19 (clone 6D5, Biolegend), NK-1.1 (clone PK136, Biolegend), Granzyme B (clone GB11, Biolegend), IFN-γ

(clone XMG1.2, Biolegend), CD3 (clone 17A2, Biolegend), CD40 (clone 5C3, Biolegend), MHCII (clone M5/114.15.2, Biolegend) and CD45 (clone HI30, Biolegend). Surface stain was performed for 45-60 minutes at 4°C. In the final 5 minutes of staining, intracellular fixation buffer was added and washed with MB. For intracellular cytokine staining, cells were first fixed with 1x Fix/Perm buffer (eBioscience Foxp3 kit) for 1 hour on ice. Intracellular stain was performed overnight at 4°C. Following washing the cell preparations were filtered on 70 µM nylon mesh and samples were analysed on flow cytometers (BD Celesta). Data was analysed using FlowJo software (Tristar).

Results

DSS induced colitis alters the faecal microbiome

Sequencing of faecal samples identified changes in the relative abundance of bacterial phyla and genera between day 0 and day 7 of the experiment when mice were treated with 3% DSS (Fig. S1). Firmicutes and Bacteroidota remained the most abundant phyla in the 3% DSS treated group, however microbial diversity was reduced with an increase in the abundance of Proteobacteria. Genera including *Clostridium, Escherichia, Lactobacillus, Parabacteroides, Bacteroides* and *Sutterella* were increased in DSS treated mice, with *Ruminococcus, Prevotella, Lachnospiraceae* and *Faecalibacterium* reduced.

Spatial metabolomic mapping of the murine ileum and colon during DSS-induced intestinal colitis

MSI was employed to elucidate molecular changes across a range of intestinal and systemic sites during DSS induced colitis. The mass spectra were acquired in the range *m/z* 50-1000 Da to identify metabolites and lipids. For each tissue type, ROC analysis was performed to identify metabolites which discriminate between control and DSS-treated mice. Unsupervised and supervised multivariate analysis was then performed on these metabolites to identify those which contributed most to the separation of the treatment groups (metabolites with a high VIP score from PLS-DA analysis). Finally, univariate analysis was performed to further validate the metabolite differences between the groups. Metabolites with a VIP score >1 and/or a *p* value of <0.05 are reported. In the ileum, multivariate and univariate analysis identified 88 metabolites significantly changed by DSS treatment (Fig. S2 and Supplementary Tables 3 and 4). Of these 49 metabolites (55.6%) could be putatively identified using the Human Metabolome Database (HMDB) (Fig. 1A). In the colon, (Fig. S3 and Supplementary Tables 5 and 6) univariate analysis indicated that 3 metabolites were significantly decreased, and 27 metabolites were significantly increased in the 3% DSS group compared to the control. Twenty of these metabolites could be assigned a putative identity (Fig. 1B). While a very large number of metabolites were putatively

identified in this study not all could have their identities confirmed by MSMS. However, MSMS was used to confirm the molecular identities of a number of metabolites by matching spectra available online these included; *m/z* 132.07-creatine, *m/z* 162.11-carnitine, *m/z* 259.24-arachidonic acid, *m/z* 327.23-docosahexaenoic acid (DHA), *m/z* 317.21-leukotriene A4 and *m/z* 351.21, lipoxin A4 and gamma-linolenic acid (GLA).

KEGG Pathway enrichment analysis of significantly changed metabolites

Given the large number of metabolites changed across the intestine, KEGG pathway enrichment analysis was conducted to identify specific pathways significantly altered by DSS treatment. Enrichment of 12 pathways was noted in the ileum of DSS treated mice, but only the arachidonic acid, steroid hormone biosynthesis and primary bile acid biosynthesis pathways were significantly enriched (Fig. S4). Fourteen KEGG pathways were identified through enrichment analysis in the colon, but again only the arachidonic acid metabolism pathway was significantly so (Fig. S5).

Mapping the effects of identified metabolites on the intestinal immune response

To better understand cellular and functional changes in the intestinal immune response post-DSS treatment, imaging mass cytometry (IMC) was employed. To guide this analysis the locations of specific metabolites, identified as significantly changed in response to DSS treatment, were used as a guide. This approach would thus identify areas of significant molecular changes due to DSS-induced colitis and probe changes in the functionality and metabolism of cells at those locations. As 128 metabolites were found to be changed in the ileum and colon during 3% DSS treatment, metabolites were selected that were significantly changed by DSS treatment that had 3 characteristics; an interesting spatial distribution, a VIP>1, and had their identities confirmed by MSMS. Metabolites that fitted these criteria were docosahexaenoic acid (DHA) (*m/z* 327.233, VIP=1.057), which was increased 2.66-fold (p=0.00197), creatine (*m/z* 132.0771, VIP=1.050) which was increased 2.29-fold (p=0.0054) in the ileum, and lastly 1-methylnicotinamide (1-MNA) (*m/z* 137.071, VIP=1.605) which increased 2.59-fold (p=0.001162) in the colon (Fig. 2). IMC was performed at a 1 μM spatial resolution (on tissue regions indicated by blue rectangular boxes in Fig. 2), revealing changes in structural and immune protein markers. Individual cells were segmented and a random forest machine learning tissue classifier segmented the colon and ileum into mucosa and muscularis regions. In the ileal mucosa, the percentage of cells positive for a number of markers were decreased, each approximately 2-fold, in the DSS-treated mice compared to controls including; F480, CD69, Ki67, CD4 and MHCII (Fig. 3). The markers identified via IMC were grouped to define single-cell phenotype and function such as proliferation, apoptosis, and activation state. In the ileal mucosa post-DSS treatment, there was a

decrease in helper T cells ($CD3^+$, $CD4^+$), dendritic cells ($CD11c^+$, $MHCII^+$), M2b macrophages and M1 macrophages ($F480^+$), and proliferative cells ($Ki67^+$)(Fig. 4). While no individual markers were significantly changed in the ileal muscularis of 3% DSS treated mice compared to control mice, the M1 macrophage population decreased 2.81-fold (p=0.0319) post-treatment.

In the colonic mucosa, 20 markers of cellular function, proliferation and structure were altered between the 3% DSS treated group and the control (Fig. 5). Those markers that decreased included ATPase, Pan-CK, CD103, CD11c, E Cadherin, Glut1, Ki67 and EpCAM, with each decreasing approximately 5-fold or less. Significant, and larger, fold increases were seen in number of markers post-DSS treatment including vimentin, CD68, Ly6G, CD11b, F480, CD163, collagen, Lyve1, FoxP3, NKp46, CD4, and granzyme B. However, in the case of Ly6G and CD68 these increases were far larger than the others at approximately 20-fold and 40-fold increases, respectively. The abundance of these markers was used to then predict the dysregulation of 14 cellular phenotypes and functions in DSS-treated mice. The percentage of positive cells that were proliferative ($Ki67^+$), hypoxic ($Glut1^+$), or antigen-presenting dendritic cells ($CD11c^+$, $MHCII^+$, $CD103^+$) was significantly reduced in the colonic mucosa of the DSS-treated mice (Fig. 6). In contrast the percentage of a range of cellular phenotypes including helper T cells ($CD3^+$, $CD4^+$), regulatory T cells ($CD3^+$, $CD4^+$, $FOXP3^+$), natural killer (NK) cells ($NKp46^+$), neutrophils ($Ly6G^+$, $CD11b^+$), blood vessels ($CD31^+$) and mesenchymal cells ($vimentin^+$) was significantly increased after DSS treatment, with neutrophil levels increasing greater than 300-fold. The percentage of macrophages ($F480^+$, $CD68^+$, $CD11b^+$) was increased greater than 50-fold with subsets including M2c ($F480^+$, $CD163^+$), M2a ($F480^+$, $CD206^+$), M2b ($F480^+$) and M1 ($F480^+$, $MHCII^+$) all contributing through their own significant fold change increase in the colonic mucosa post-DSS treatment. In the colonic muscularis of the 3% DSS-treated group, the percentage of $CD11b^+$ (8.24-fold, p<0.0001), $F480^+$ (7.20-fold, p=0.0008) and granzyme B^+ (7.00-fold, p=0.0234) cells increased compared to the control, while the percentage of M2c (6.15-fold, p=0.0009), M1 and M2 macrophages (7.20-fold, p=0.0008), and M1 macrophage positive cells (3.85-fold, p=0.0419) again all significantly increased in a manner similar to that observed in the mucosa of the 3% DSS treated group.

Effects of specific metabolites on immune response

To further elucidate how the metabolites utilized to select regions for IMC may be contributing to the altered immune profile, these metabolites creatine, DHA and 1-MNA, were used to conduct a variety of *in vitro* tests. Firstly, to confirm their identity MSMS spectra for creatine, DHA and 1-MNA standards were collected alongside tissue spectra. All tissue spectra closely matched their standards as they share peaks at similar abundances,

indicating that they are the same molecule (Fig. S6A-C). Lactate dehydrogenase and caspase-3 activity assays indicated that creatine, DHA and 1-MNA have cytotoxic effects on intestinal epithelial cells but do not induce apoptosis (Fig. S7). Cytokine release in response to the metabolites varied, but none of the metabolites resulted in IL-6 release (Fig. S8). 50 μM creatine or 100 μM DHA significantly reduced IL-8 release while 100 μM DHA was observed to significantly increase the release of TNF-α. Increasing the concentration of creatine, DHA and 1-MNA to 100 μM, from 50 μM, resulted in increased release of IL-15 in response to all the metabolites (Fig. S8).

After determining that creatine and DHA have an immunomodulatory effect on IECs we next established their effect on immune cells. Immune cells were isolated from mouse spleens and stimulated with creatine, DHA, or a cytokine control (IL-4 or IL-12+IL-18). Gating strategy is as described in Fig. S9. While DHA did not significantly change the percentage of any immune cell type, stimulating cells with creatine increased the percentage of NK cells expressing CD69 (2.67-fold, p=0.0007)(Fig. 7). A proteome profiler mouse cytokine array indicated that IFN-γ was increased in the cell supernatant following molecular exposure and IFN-γ levels were quantified by ELISA. Creatine treatment did not significantly alter IFN-γ release compared to the control but treating cells with DHA increased the secretion of IFN-γ 13-fold (p<0.0001)(Fig. 7).

Spatial metabolomic mapping of the murine liver, spleen and kidney during DSS-induced intestinal colitis

Given the changes in metabolite abundance seen in the intestine post-treatment of mice with 3% DSS, systemic metabolomic changes were determined through MSI of the liver, spleen, kidney and lung. Univariate analysis after MSI of the liver indicated that 239 metabolites were significantly changed post-DSS treatment and putative identities could be assigned to 125 metabolites (52.3%) (Fig. S10 and Supplementary Tables 7 and 8). Given the large number of metabolites identified in the liver these could not be shown as a heatmap. In the spleen univariate statistical analysis identified 65 peaks that were significantly changed but only 34 molecules (51.5%) could be assigned a putative identity (Fig. S11 and Supplementary Tables 9 and 10). Metabolites significantly changed in the spleen are shown as a heatmap (Fig. 8). In the kidney of the DSS colitis model 16 metabolites were found to be significantly changed between the groups following univariate analysis (Fig. S12 and Supplementary Tables 11 and 12) and are shown in a heatmap (Fig. 9). This study could assign 11 putative identities to the metabolites using the HMDB. MSI was also performed on lung tissue but no significantly changed metabolites were found between control and 3% DSS treated animals.

KEGG enrichment analysis indicated that the metabolites found in the liver dataset are involved in at least 25 pathways (Fig. S13) but only the galactose metabolism and biosynthesis of unsaturated fatty acids pathways were significantly enriched. No significantly enriched pathways were identified in the spleen (Fig. S14), and in the kidney the small number of identified metabolites prevented KEGG pathway analysis being informative.

Identification of putative biomarkers of intestinal colitis at systemic sites

We aimed to identify molecular biomarkers of intestinal inflammation that were also altered at systemic sites which may contribute to systemic inflammation. To guide this approach we identified metabolites that were significantly changed in abundance at both intestinal and systemic sites. A number of metabolites were significantly altered in both the ileum and colon in response to DSS. These included metabolites increased in both tissues such as 11b-hydroxyandrost-4-ene-3,17-dione (*m/z* 301.1658; ileum 15.8-fold, *p*=0.03; colon 4.84-fold, *p*=0.001), ubiquinone-2 (*m/z* 317.1759; ileum 3.06-fold, *p*=0.0012; colon 7.9-fold, *p*=0.02), epoxydocosapentaenioc acid (*m/z* 343.228; ileum 3.40-fold, *p*=0.0038; colon 7.1-fold, *p*=0.02) and 14-hydroperoxy-H4-neuroprostane (*m/z* 391.2126; ileum 4.45-fold, *p*=0.0019; colon 12.64-fold, *p*=0.023). Or metabolites such as *m/z* 277.2172, putatively identified as gamma-linolenic acid, which was significantly decreased in the colon (2.09-fold, *p*=0.045) and ileum (2.11-fold, *p*=0.0012) post-DSS treatment. Lastly, the metabolites with *m/z* 193.1234 and *m/z* 221.1183 were significantly increased in both the ileum (1.78-fold, *p*=0.0019) and colon (2.32-fold, *p*=0.0239) of DSS treated mice but no putative identity could be assigned to them.

When focusing on systemic metabolites of interest, ubiquinone-2 was increased in the liver of DSS treated mice in a manner similar to that seen in the intestine (2.73-fold, *p*=0.00108), while gamma-linolenic acid was similarly decreased (1.67-fold, *p*=0.0016) (Fig. 10). A further 7 metabolites were found to be common and similarly altered in both the liver and ileum. Carnitine (*m/z* 162.1138) was found to be significantly increased in both liver (3.73-fold, *p*=0.0034) and in the ileum (1.57-fold, *p*=0.0098) of DSS treated mice. A further five metabolites were significantly altered but were all decreased in abundance in the ileum and liver of the DSS-treated mice. Fatty acyl esters of hydroxy fatty acid (FAHFA) (*m/z* 509.4583; ileum 3.91-fold, *p*=0.0019; liver 3.35-fold, *p*=0.00014) and a diglyceride (DG(34:1))(*m/z* 607.4946; ileum 3.18-fold, *p*=0.00233; liver 4.38-fold, *p*=0.00007) could be assigned putative identities but *m/z* 511.4731 (ileum 1.98-fold, *p*=0.001; liver 1.50-fold, *p*=0.000435), *m/z* 512.4757 (ileum 2.18-fold, *p*=0.0019; liver 1.53-fold, *p*=0.000405) and *m/z* 583.4945 (ileum 5.09-fold, *p*=0.001; liver 8.88-fold, *p*=0.0001) all remained unknowns. Lastly a diglyceride (DG(18:0)) (*m/z* 594.34087) was the only metabolite to show a significant decrease in the

ileum (3.70-fold, *p*=0.00190) but a significant increase (2.17-fold, *p*= 0.00235) in the liver after DSS treatment.

In the spleen and colon 7 metabolites were found to be altered at both sites during DSS-induced colitis. *m/z* 160.1334 was putatively identified as 5-AVAB, but may be other microbiome-derived metabolites as a number have an identical *m/z* (22, 23). This *m/z* was significantly decreased in the spleen (1.63-fold, *p*=0.028) and in the colon (1.81-fold, *p*=0.02) of DSS treated mice (Fig. 11). Six other metabolites were significantly increased in both the spleen and colon of 3% DSS treated mice. These metabolites were putatively identified as octadecatriencoic acid (2.04-fold colon, *p*=0.04; 1.54-fold spleen, *p*=0.0003), 11b-hydroxyandrost-4-ene-3,17-dione (15.8-fold colon, *p*=0.03; 4.65-fold spleen, *p*=0.04), ubiquinone-2 (7.9-fold colon, *p*=0.02; 3.38-fold spleen, *p*=0.005), epoxydocosapentaenoic acid (7.1-fold colon, *p*=0.02; 2.37-fold spleen, *p*=0.0016), resolvin D5 (19.0-fold colon, *p*=0.02; 2.28-fold spleen, *p*=0.0058) and resolvin D1 (19.14-fold colon, *p*=0.02; 2.26-fold spleen, *p*=0.0062)). Five metabolites were similarly altered in the ileum and spleen. Three of these metabolites, described above, are 11b-hydroxyandrost-4-ene-3-17-dione, ubiquinone-2 and epoxydocosapentaenoic acid and these were increased in the spleen 4.8-fold (*p*=0.0019), 3.06-fold (*p*=0.0012) and 3.4-fold (*p*=0.0038), respectively. The remaining two upregulated metabolites, which could not be assigned identities, have *m/z* 251.2016 (2.13-fold ileum, *p*=0.0013; 1.58-fold spleen, *p*=0.0091) and *m/z* 328.2364 (2.66-fold ileum, *p*=0.0012; 2.62-fold, *p*=0.0391).

The molecule putatively identified as gamma-linolenic acid was significantly changed in the ileum, colon, and liver in the colitis model. Again gamma-linolenic acid was also found to be significantly decreased 2.03-fold (*p*=0.016) in the kidney of the 3% DSS treated group compared to the controls (Fig. 12). The molecule with *m/z* 865.5019 was putatively identified as a phosphatidylglyceride (PG(38:4)) and was found to be upregulated in the ileum (4.52-fold, *p*=0.0028) and kidney (14.5-fold, *p*=0.0259) during DSS colitis compared to the control. Lastly, the molecule with *m/z* 305.2481 was putatively identified as dihomo-gamma-linolenic acid. This molecule was significantly increased (1.96-fold, *p*=0.0019) in the ileum and decreased in the kidney (1.71-fold, *p*=0.0156) in the DSS treated group compared to the controls.

Intestinal colitis results in a dysregulated immune cell profile in the liver

As MSI revealed hundreds of metabolite changes in the liver during colitis, IMC was employed for single-cell phenotyping to identify changes in function. As MSI heatmaps indicated that, unlike in the intestine most metabolites were homogenous throughout liver tissue, the sections were selected for IMC at random. The liver was segmented into regions, tissue and blood vessels based on tissue morphology. In the tissue of the 3% DSS treated

group, the percentage of $CD68^+$, $CD45^+$, $F480^+$, $CD163^+$, E $cadherin^+$, $collagen^+$, $Glut1^+$ and $CD206^+$cells increased (Fig. 13). The markers identified were used to predict changes in specific cell types and the results showed that in the 3% DSS treated group, the percentage of regulatory T cells ($CD3^+$, $CD4^+$, $FOXP3^+$) and activated cytotoxic T cells ($CD3^+$, $CD8^+$, Granzyme B^+) was significantly reduced 2.44-fold (p=0.0493) and 14.42-fold (p=0.0244), respectively, compared to controls. However, the percentage of macrophage cells in the subclass M2c ($F480^+$, $CD163^+$) and M2a ($F480^+$, $CD206^+$) were significantly increased 2.42-fold (p=0.0050) and 2.32-fold (p=0.0018), respectively, in the 3% DSS treated group. Lastly, the percentage of cells that were hypoxia positive ($Glut1^+$) increased 2.03-fold (p=0.0271) during treatment compared to the control (Fig. 14).

In liver vessels, the percentage of cells expressing the following markers increased in the 3% DSS treated group compared to controls; CD68 (2.50-fold, p=0.0346), F480 (2.25-fold, p=0.0005), CD11b (2.25-fold, p=0.0396), CD163 (2.98-fold, p=0.0169), E Cadherin (1.83-fold, p=0.0162), Lyve1 (2.29-fold, p=0.0179), NKp46 (1.07-fold, p=0.0221), CD206 (1.51-fold, p=0.0092), Glut1 (1.38-fold, p=0.0044) and ATPase (1.04-fold, p=0.0006), respectively. Furthermore, the percentage of M2c (3.26-fold, p=0.0081) and M2a (2.73-fold, p=0.0005) macrophage positive cells significantly increased and, respectively, in the 3% group compared to controls. Furthermore, the vessel in DSS-treated mice had a 1.38-fold (p=0.0044) increase in the percentage of cells positive for hypoxia. This indicates that during intestinal colitis the liver undergoes injury via hypoxia.

Discussion:

The gut microbiome exerts its effects through direct interactions with the intestinal epithelium and through the release of countless metabolites that exert their both locally and systemically. Here, using a spatial biology approach to understand molecular and cellular localization, we gained an understanding of the influence of disruption of the gut microbiota and intestinal inflammation in the commonly used DSS colitis model.

In DSS treated mice the arachidonic acid (AA) pathway was significantly enriched in the ileum and colon. AA is hydrolysed by phospholipase A2 (PLA_2) into a free form before breakdown to produce bioactive eicosanoids such as prostaglandins (PGs), thromboxanes (TXs), leukotrienes (LTs) and eicosatetraenoic acids (ETEs)(24-26). Some such as the LT, leukotriene B4 (LTB_4), are potent chemoattractants being the main mediator in neutrophil recruitment (27).

The AA pathway was enriched in the ileum and colon but there were differences in the metabolites detected at each site. In the ileum 20(S)-HETE, prostaglandin G2 (PGG_2), thromboxane B2 and LTB_4 were increased in colitis, whereas 11,12-EET, 15S-HETE and 5(S)-HETE were increased in the colon. It is likely that these influence the distinctive cellular

profiles seen at each site by IMC (28). For example, 5(S)-HETE is synthesized by neutrophils in response to infection, eliciting a strong pro-inflammatory response by increasing transepithelial neutrophil chemotaxis (29). 5(S)-HETE can subsequently increase neutrophil degranulation releasing anti-bacterial products and reactive oxygen species (ROS) contributing to further dysbiosis, tissue injury and inflammation (30). Our cellular phenotyping indicates helper T cells, dendritic cells, M2b and M1 macrophages, and proliferation positive cells were decreased, in the ileal mucosa of DSS mice suggesting an anti-inflammatory or pro-resolving state (31, 32). Further evidence for this is demonstrated by an increase in the AA derivative lipoxin A4 (LXA_4), a pro-resolving and anti-inflammatory eicosanoid mediator (33, 34). LXA_4 is produced instead of LTB_4 after neutrophils are exposed to prostaglandins via the induction of 15-LOX, which acts as a signal to stop further neutrophil recruitment (35). The presence of this molecule indicates that the ileum is in a resolution phase and that specific derivatives of the AA pathway might be contributing to the anti-inflammatory environment.

While only the AA pathway was enriched in the colon, the steroid hormone biosynthesis and primary bile acid biosynthesis pathways were also enriched in the ileum. These pathways overlap with both involving 25-hydroxycholesterol and dihydroxy-cholesterols, which were increased in the DSS treated mice. 25-hydroxycholesterol can have dual functionality, exerting both pro- and anti-inflammatory effects (36, 37). It can enhance B cell secretion of IL-8 and Il-6, and lipopolysaccharide treated macrophages increase 25-hydroxycholesterol production which correlates with increased cytokine C-C Motif chemokine Ligand 5 expression (CCL5) (38). Increased expression of these cytokines and CCL5 promotes immune cell infiltration to injured sites exacerbating inflammation. However, our data does not suggest the ileal mucosa was overcome with immune cell infiltrate and it appears more likely that 25-hydroxycholesterol is exerting a pro-resolving effect. 25-hydroxycholesterol decreases the production of the potent proinflammatory cytokine IL-1β which promotes the recruitment and retention of macrophages (37). Therefore, it is likely that the significant decrease in macrophage subsets in the ileal mucosa may be due to 25-hydroxycholesterol-driven attempts at resolution of inflammation.

In contrast in the inflamed colonic mucosa cells that were proliferative, hypoxic, and antigen-presenting dendritic cells were significantly reduced, whereas helper T cells, regulatory T cells, NK cells, neutrophils and macrophages were all increased. NK cells, macrophages and neutrophils play roles in CD progression by producing large quantities of proinflammatory cytokines including TNF-α, IL-6 and IL-8 (39, 40). Moreover, antigen-presenting dendritic cells are pivotal in the balance between tolerance and active immunity towards commensals, thus their decreased presence in the inflamed mucosa may be contributing to microbial exacerbation of DSS-induced inflammation (551). This suggests

that the differences in cellular function between the colon and ileum during DSS-induced colitis is likely heavily influenced by specific metabolites and targeting these is likely to have an impact as a potential future therapeutic approach.

Creatine, DHA and 1-MNA were significantly increased in DSS-treated mice and were significant drivers in separating the clusters of DSS-treated mice and controls, suggesting they play an important role the inflammatory response. DHA is a precursor of the anti-inflammatory docasanoids, known as resolvins (Rv), protectins (PD) and maresins (Ma) anti-inflammatory properties, resulting in the downregulation of pro-inflammatory AA-derived prostaglandins and leukotrienes actively promoting resolution (41, 42). Increased DHA in the ileum corresponds with a decrease in helper T cells, dendritic cells, and M2b and M1 macrophages, suggesting DHA is important for resolving colitis, most likely through its degradation to pro-resolving mediators (43). DHA increased splenic immune cell secretion of IFN-γ *in vitro*, and with aberrant production of IFN-γ a major driver of IBD, this is likely contributing to an excessive immune response resulting in mucosal infiltration and damage. Thus, DHA activation of IFN-γ production may be a major contributor to intestinal pathology (44). While DHA has been described in the literature as having pro-inflammatory properties the likely outcomes of DHA presence are dependent on whether it is further degraded to anti-inflammatory end products. If DHA accumulates in the intestine without being metabolised to anti-inflammatory derivatives, it may significantly contribute to inflammation, something which needs to be fully considered given it has been suggested as an IBD therapeutic.

Clostridia and *Escherichia* were enriched in this study's faecal microbiome during DSS colitis, since these bacteria metabolise creatine, the increase in creatine availability may underlie this dysbiotic expansion with resulting impacts on immunometabolism (45). The creatine phosphate shuttle is increased in epithelial cells during DSS-induced metabolic stress, so the observed increase in creatine levels in the DSS-treated ileum might be a metabolic response in an attempt to restore cellular energy (46). Creatine supplementation in DSS colitis reduces disease severity and improves barrier function, thus the use of creatine in IBD patients has been suggested (47). Creatine supplementation reduces the secretion of TNF-α from macrophages, dampening the M1 inflammatory response (48). Our data loosely supports this as IMC revealed a reduction in cells with a macrophage-like phenotype in the ileum when creatine was increased.

CD69 expression is essential to the onset of inflammation in IBD and commensal microorganisms play a critical role in modulating CD69 expression by intestinal lymphocytes as mice depleted of microflora have reduced CD69 levels (49, 50). CD69 is a proinflammatory molecule as it is an important regulator of intestinal immune responses particularly at mucosal sites inducing Ca^{2+} influx and lymphocyte proliferation as well as the

production of potent inflammatory mediators such as TNF-α (51, 52). Given its clear importance in inflamed areas of the intestine and its ability to stimulate NK cells, creatine is worthy of further investigation to assess its role in IBD.

In the colon, 1-MNA was also identified as increased in the inflamed mucosa and was an important metabolite in clustering and separation of the inflamed from the control tissues. Increased 1-MNA has been described as hepatoprotective in liver inflammation as it can exert an anti-inflammatory effect observed as suppression of IL-4 and TNF-α immune cell signalling (53, 54). 1-MNA was seen here to reduce production of IFN-γ, something previously seen in $CD4^+$ T cells (55). $CD4^+$ T cell production of IFN-γ is essential for bactericidal activity against many microbes (56). Therefore, 1-MNA suppression of IFN-γ may result in impaired bacterial clearance, contributing to dysbiosis.

As primary bile acid biosynthesis was enriched in the ileum of the DSS-induced colitis model, it was expected that bile acid pathways would be significantly altered in the liver due to the gut-liver axis. However, this was not the case and the most significantly enriched pathway was galactose metabolism. Galactose is hydrolysed from ingested lactose in the intestine and travels to the liver where it is metabolised exclusively (57). Glucose transporter 1 (Glut1), was significantly increased in the liver of mice with colitis, compared to the control. Glut1 is translocated to hepatic cell membranes, to increase glucose uptake during stress, such as bacterial infection (58). This implies that glucose availability in the liver during DSS-induced colitis is reduced, resulting in increased D-galactose metabolism and Glut1 expression, in an attempt to salvage the liver energy supply (59-61).

The pathway for biosynthesis of unsaturated fatty acids pathway was also enriched in the liver. This pathway resulted in a decrease in the abundance of gamma-linolenic acid (GLA) in the liver, ileum, colon, and kidney of colitis mice. GLA is an omega-6, 18 carbon PUFA, that is consumed in the diet (62). GLA is rapidly enzymatically converted into dihomo-gamma-linolenic acid (DGLA) and due to continuous conversion, it is naturally found at low levels with a corresponding increase in DGLA (63). Liver cells, have the capacity to desaturate DGLA to form AA, increasing the production of proinflammatory eicosanoids such as PGs, TXs and LTs and resulting in a decrease in DGLA (30, 64, 65). In agreement, AA was increased in the liver of colitis mice suggesting that GLA and DGLA are potentially used as precursors for AA production, skewing the DGLA/ AA balance to support inflammation (64, 65). Furthermore, this study putatively identified prostaglandin G2 (PGG_2), an AA derivative, as being increased in the colitis liver and has been implicated as a pathophysiological factor in liver cirrhosis by promoting platelet aggregation and thrombosis (66). Therefore, the bidirectional liver-gut axis may exacerbate inflammation and tissue damage in both organs via AA production and conversion to small metabolites meaning the

disappearance of the precursor GLA could be used as a biomarker of systemic disease progression (65, 67).

Other metabolites were putatively identified and similarly altered between tissue types that could potentially be biomarkers of disease and warrant further investigation. Ubiquinone-2, also known as coenzyme Q2 (COQ2), is the second of at least ten functional proteins involved in the biosynthesis of endogenous coenzyme Q10 (CoQ10) was increased in the ileum, colon, liver, and spleen of DSS-treated mice (68). Within mitochondria, CoQ10 acts as an electron carrier that increases the generation of ATP via oxidative phosphorylation (69). In addition, CoQ10 can be reduced to ubiquinol, which has been shown to have strong antioxidant and anti-inflammatory properties (70). During LPS induced stress, ubiquinol treatment blocks protein kinase C (PKC) activity and improves mitochondrial function, preventing ROS generation and cellular damage (71). CoQ10 supplementation in UC patients, also decreased the severity of inflammation and reduced blood pressure (72). As ubiquinone-2 was increased in the intestine, liver, and spleen, it can be suggested that increasing biosynthesis or supplementation would not only reduce inflammation in the intestine but could have a systemic protective effect, increasing its usefulness as a therapeutic target (71-73). The molecule putatively identified as epoxydocosapentaenoic acid (EDP) was increased in the ileum, colon, and spleen of colitis mice. This is a naturally occurring bioactive derivative of DHA, derived via cytochrome P450 epoxygenses (74). To our knowledge, research has largely overlooked this molecule as focus has been on DHA, but, EDP also has anti-inflammatory potential (74, 75). EDP is increased in circulation of breast cancer patients following DHA supplementation and has a positive effect on patient prognosis (76, 77). This has been attributed to EDP ability to inhibit angiogenesis, suppress endothelial cell migration, and primary tumour growth (78). Furthermore, EDP can reduce the expression of TNF-α and TNF-α-induced leukocyte adhesion in Müller cells and retinal endothelial cells, thus it may be useful in treating inflammatory eye conditions (75). Therefore, the increased EDP in the intestine and spleen may exert an anti-inflammatory protective effect and warrants further investigation as an intestinal and systemic inflammatory therapeutic target.

In conclusion, DESI MSI can be employed to discover metabolites derived by the host and microbiome that could play a role in the onset and progression of DSS-induced colitis. The study revealed numerous molecular pathways and specific molecules, such as creatine, DHA and 1-MNA, have immunomodulatory effects and have the potential to perpetuate inflammation within the intestinal mucosa. Furthermore, the study shows that specific metabolites are altered in the liver, spleen and kidney during inflammation and have the potential to drive pro and anti-inflammatory mechanisms. Some of these metabolites such as GLA may result in systemic disease manifestations and may be new targets for therapeutic

intervention. Lastly, some metabolites such as ubiquinone-2 and EDP are present in multiple tissue including the intestine during colitis; thus, if used as therapeutic target could dampen both intestinal and systemic inflammation.

Conflict of interest:

The authors declare that there are no conflicts of interest.

Funding:

This work was supported in part by UKRI Biotechnology and Biological Sciences Research Council (BBSRC) grant number BB/V001876/1 to R.B., R.G. and DMW. L.A. was funded through a joint University of Glasgow AstraZeneca BBSRC Industrial CASE partnership PhD studentship.

Data availability:

The data that support the findings of this study are available from the corresponding author upon reasonable request.

Bibliography:

1. Luzoro A, Sabat P, Guzmán L, Frias F. Extraintestinal Manifestations of Inflammatory Bowel Disease. Gastroenterology & Hepatology. 2011;7(4):235-.
2. Sartini A, Gitto S, Bianchini M, Verga MC, Girolamo MD, Bertani A, et al. Non-alcoholic fatty liver disease phenotypes in patients with inflammatory bowel disease. Cell Death & Disease 2018 9:2. 2018;9(2):1-8.
3. Okayasu I, Hatakeyama S, Yamada M, Ohkusa T, Inagaki Y, Nakaya R. A novel method in the induction of reliable experimental acute and chronic ulcerative colitis in mice. Gastroenterology. 1990;98(3):694-702.
4. Massafra V, Ijssennagger N, Plantinga M, Milona A, Pittol JMR, Boes M, van Mil SWC. Splenic dendritic cell involvement in FXR-mediated amelioration of DSS colitis. Biochimica et Biophysica Acta (BBA) - Molecular Basis of Disease. 2016;1862(2):166-73.
5. Xie D, Li F, Pang D, Zhao S, Zhang M, Ren Z, et al. Systematic Metabolic Profiling of Mice with Dextran Sulfate Sodium-Induced Colitis. Journal of Inflammation Research. 2021;14:2941-.
6. Yazbeck R, Howarth GS, Butler RN, Geier MS, Abbott CA. Biochemical and histological changes in the small intestine of mice with dextran sulfate sodium colitis. Journal of Cellular Physiology. 2011;226(12):3219-24.

7. Chassaing B, Aitken JD, Malleshappa M, Vijay-Kumar M. Dextran Sulfate Sodium (DSS)-Induced Colitis in Mice. Current protocols in immunology / edited by John E Coligan [et al]. 2014;104(SUPPL.104):Unit-Unit.

8. Guan Q. A Comprehensive Review and Update on the Pathogenesis of Inflammatory Bowel Disease. Journal of Immunology Research. 2019;2019.

9. Kim SH, Kwon D, Son SW, Jeong TB, Lee S, Kwak JH, et al. Inflammatory responses of C57BL/6NKorl mice to dextran sulfate sodium-induced colitis: comparison between three C57BL/6 N sub-strains. Lab Anim Res. 2021;37(1):8.

10. Hernández-Chirlaque C, Aranda CJ, Ocón B, Capitán-Cañadas F, Ortega-González M, Carrero JJ, et al. Germ-free and Antibiotic-treated Mice are Highly Susceptible to Epithelial Injury in DSS Colitis. Journal of Crohn's and Colitis. 2016;10(11):1324-35.

11. Park H, Yeo S, Kang S, Huh CS. Longitudinal Microbiome Analysis in a Dextran Sulfate Sodium-Induced Colitis Mouse Model. Microorganisms. 2021;9(2):1-18.

12. Zheng L, Wen XL, Duan SL. Role of metabolites derived from gut microbiota in inflammatory bowel disease. World J Clin Cases. 2022;10(9):2660-77.

13. Schmalle V, Lorentz A. Role of the microbiota in circadian rhythms of the host. Chronobiology international. 2020;37(3):301-10.

14. Cani PD, Hul MV, Lefort C, Depommier C, Rastelli M, Everard A. Microbial regulation of organismal energy homeostasis. Nature Metabolism 2019 1:1. 2019;1(1):34-46.

15. Ji Y, Gao Y, Chen H, Yin Y, Zhang W. Indole-3-Acetic Acid Alleviates Nonalcoholic Fatty Liver Disease in Mice via Attenuation of Hepatic Lipogenesis, and Oxidative and Inflammatory Stress. Nutrients 2019, Vol 11, Page 2062. 2019;11(9):2062-.

16. Ning L, Zhou YL, Sun H, Zhang Y, Shen C, Wang Z, et al. Microbiome and metabolome features in inflammatory bowel disease via multi-omics integration analyses across cohorts. Nat Commun. 2023;14(1):7135.

17. Mukhopadhyay S, Saha S, Chakraborty S, Prasad P, Ghosh A, Aich P. Differential colitis susceptibility of Th1- and Th2-biased mice: A multi-omics approach. PLOS ONE. 2022;17(3):e0264400-e.

18. Shiomi Y, Nishiumi S, Ooi M, Hatano N, Shinohara M, Yoshie T, et al. GCMS-based metabolomic study in mice with colitis induced by dextran sulfate sodium. Inflammatory Bowel Diseases. 2011;17(11):2261-74.

19. Pang Z, Chong J, Li S, Xia J. MetaboAnalystR 3.0: Toward an Optimized Workflow for Global Metabolomics. Metabolites. 2020;10(5).

20. Magoc T, Salzberg SL. FLASH: fast length adjustment of short reads to improve genome assemblies. Bioinformatics. 2011;27(21):2957-63.

21. Caporaso JG, Kuczynski J, Stombaugh J, Bittinger K, Bushman FD, Costello EK, et al. QIIME allows analysis of high-throughput community sequencing data. Nature Methods. 2010;7(5):335-6.

22. Hulme H, Meikle LM, Strittmatter N, van der Hooft JJJ, Swales J, Bragg RA, et al. Microbiome-derived carnitine mimics as previously unknown mediators of gut-brain axis communication. Science Advances. 2020;6(11):eaax6328-eaax.

23. Haikonen R, Kärkkäinen O, Koistinen V, Hanhineva K. Diet- and microbiota-related metabolite, 5-aminovaleric acid betaine (5-AVAB), in health and disease. Trends in Endocrinology & Metabolism. 2022;33(7):463-80.

24. Sala A, Proschak E, Steinhilber D, Rovati GE. Two-pronged approach to anti-inflammatory therapy through the modulation of the arachidonic acid cascade. Biochemical Pharmacology. 2018;158:161-73.

25. Wang B, Wu L, Chen J, Dong L, Chen C, Wen Z, et al. Metabolism pathways of arachidonic acids: mechanisms and potential therapeutic targets. Signal Transduction and Targeted Therapy 2021 6:1. 2021;6(1):1-30.

26. Patrono C, Rocca B. Measurement of thromboxane biosynthesis in health and disease. Frontiers in Pharmacology. 2019;10(OCT):1244-.

27. Hopke A, Lin T, Scherer AK, Shay AE, Timmer KD, Wilson-Mifsud B, et al. Transcellular biosynthesis of leukotriene B(4) orchestrates neutrophil swarming to fungi. iScience. 2022;25(10):105226.

28. Saravia J, Raynor JL, Chapman NM, Lim SA, Chi H. Signaling networks in immunometabolism. Cell Research 2020 30:4. 2020;30(4):328-42.

29. Bittleman DB, Casale TB. 5-Hydroxyeicosatetraenoic acid (HETE)-induced neutrophil transcellular migration is dependent upon enantiomeric structure. American journal of respiratory cell and molecular biology. 1995;12(3):260-7.

30. Clark SR, Guy CJ, Scurr MJ, Taylor PR, Kift-Morgan AP, Hammond VJ, et al. Esterified eicosanoids are acutely generated by 5-lipoxygenase in primary human neutrophils and in human and murine infection. Blood. 2011;117(6):2033-.

31. Middel P, Raddatz D, Gunawan B, Haller F, Radzun HJ. Increased number of mature dendritic cells in Crohn's disease: evidence for a chemokine mediated retention mechanism. Gut. 2006;55(2):220-.

32. Imam T, Park S, Kaplan MH, Olson MR. Effector T Helper Cell Subsets in Inflammatory Bowel Diseases. Frontiers in Immunology. 2018;9(JUN):1-.

33. Zhang Y, Chen H, Zhang W, Cai Y, Shan P, Wu D, et al. Arachidonic acid inhibits inflammatory responses by binding to myeloid differentiation factor-2 (MD2) and preventing MD2/toll-like receptor 4 signaling activation. Biochimica et Biophysica Acta (BBA) - Molecular Basis of Disease. 2020;1866(5):165683-.

34. Serhan CN. Pro-resolving lipid mediators are leads for resolution physiology. Nature. 2014;510(7503):92-101.
35. Serhan CN, Levy BD. Resolvins in inflammation: emergence of the pro-resolving superfamily of mediators. The Journal of Clinical Investigation. 2018;128(7):2657-.
36. Bah SY, Dickinson P, Forster T, Kampmann B, Ghazal P. Immune oxysterols: Role in mycobacterial infection and inflammation. The Journal of Steroid Biochemistry and Molecular Biology. 2017;169:152-63.
37. Reboldi A, Dang EV, McDonald JG, Liang G, Russell DW, Cyster JG. 25-hydroxycholesterol suppresses interleukin-1-driven inflammation downstream of type I interferon. Science. 2014;345(6197):679-84.
38. Diczfalusy U, Olofsson KE, Carlsson AM, Gong M, Golenbock DT, Rooyackers O, et al. Marked upregulation of cholesterol 25-hydroxylase expression by lipopolysaccharide. Journal of Lipid Research. 2009;50(11):2258-64.
39. Bittencourt VZ, Jones F, Tosetto M, Doherty GA, Ryan EJ. Dysregulation of Metabolic Pathways in Circulating Natural Killer Cells Isolated from Inflammatory Bowel Disease Patients. Journal of Crohn's & colitis. 2021;15(8):1316-25.
40. Mattos BRRD, Garcia MPG, Nogueira JB, Paiatto LN, Albuquerque CG, Souza CL, et al. Inflammatory Bowel Disease: An Overview of Immune Mechanisms and Biological Treatments. Mediators of Inflammation. 2015;2015.
41. Marion-Letellier R, Savoye G, Beck PL, Panaccione R, Ghosh S. Polyunsaturated Fatty Acids in Inflammatory Bowel DiseasesA Reappraisal of Effects and Therapeutic Approaches. Inflammatory Bowel Diseases. 2013;19(3):650-61.
42. Tabbaa M, Golubic M, Roizen MF, Bernstein AM. Docosahexaenoic Acid, Inflammation, and Bacterial Dysbiosis in Relation to Periodontal Disease, Inflammatory Bowel Disease, and the Metabolic Syndrome. Nutrients. 2013;5(8):3299-.
43. Kong W, Yen JH, Ganea D. Docosahexaenoic acid prevents dendritic cell maturation, inhibits antigen-specific Th1/Th17 differentiation and suppresses experimental autoimmune encephalomyelitis. Brain, behavior, and immunity. 2011;25(5):872-82.
44. Langer V, Vivi E, Regensburger D, Winkler TH, Waldner MJ, Rath T, et al. IFN-gamma drives inflammatory bowel disease pathogenesis through VE-cadherin-directed vascular barrier disruption. J Clin Invest. 2019;129(11):4691-707.
45. Lee JS, Wang RX, Alexeev EE, Colgan SP. Intestinal Inflammation as a Dysbiosis of Energy Procurement: New Insights into an Old Topic. Gut Microbes. 2021;13(1):1-20.
46. Turer E, McAlpine W, Wang KW, Lu T, Li X, Tang M, et al. Creatine maintains intestinal homeostasis and protects against colitis. Proceedings of the National Academy of Sciences of the United States of America. 2017;114(7):E1273-E81.

47. Glover LE, Bowers BE, Saeedi B, Ehrentraut SF, Campbell EL, Bayless AJ, et al. Control of creatine metabolism by HIF is an endogenous mechanism of barrier regulation in colitis. Proceedings of the National Academy of Sciences of the United States of America. 2013;110(49):19820-5.

48. Riesberg LA, McDonald TL, Wang Y, Chen XM, Holzmer SW, Tracy SM, Drescher KM. Creatinine downregulates TNF-α in macrophage and T cell lines. Cytokine. 2018;110:29-38.

49. Hasegawa A, Iwamura C, Kitajima M, Hashimoto K, ichiro Otsuyama K, Ogino H, et al. Crucial Role for CD69 in the Pathogenesis of Dextran Sulphate Sodium-Induced Colitis. PLOS ONE. 2013;8(6):e65494-e.

50. Radulovic K, Manta C, Rossini V, Holzmann K, Kestler HA, Wegenka UM, et al. CD69 Regulates Type I IFN-Induced Tolerogenic Signals to Mucosal CD4 T Cells That Attenuate Their Colitogenic Potential. The Journal of Immunology. 2012;188(4):2001-13.

51. Sancho D, Santis AG, Alonso-Lebrero JL, Viedma F, Tejedor R, Sánchez-Madrid F. Functional Analysis of Ligand-Binding and Signal Transduction Domains of CD69 and CD23 C-Type Lectin Leukocyte Receptors. The Journal of Immunology. 2000;165(7):3868-75.

52. Borrego F, Robertson MJ, Ritz J, Peña J, Solana R. CD69 is a stimulatory receptor for natural killer cell and its cytotoxic effect is blocked by CD94 inhibitory receptor. Immunology. 1999;97(1):159-.

53. Sternak M, Jakubowski A, Czarnowska E, Slominska EM, Smolenski RT, Szafarz M, et al. Differential involvement of IL-6 in the early and late phase of 1-methylnicotinamide (MNA) release in Concanavalin A-induced hepatitis. International Immunopharmacology. 2015;28(1):105-14.

54. Sternak M, Khomich TI, Jakubowski A, Szafarz Mg, Szczepañski W, Bia³as M, et al. Nicotinamide N-methyltransferase (NNMT) and 1-methylnicotinamide (MNA) in experimental hepatitis induced by concanavalin A in the mouse Abbreviations: ALT-alanine aminotransaminase, INFg-inter-feron-g, Met-2PY-1-methyl-2-pyridone-5-carboxamide, Met-4PY-1-methyl-4-pyridone-5-carboxamide, MNA-1-methyl-nicotinamide, NA-nicotinamide, NNMT-nicotinamide N-methyltransferase, TNFa-tumor necrosis factor-a. Pharmacological Reports. 2010;62:483-93.

55. Kilgour MK, MacPherson S, Zacharias LG, Ellis AE, Sheldon RD, Liu EY, et al. 1-Methylnicotinamide is an immune regulatory metabolite in human ovarian cancer. Science Advances. 2021;7(4).

56. Green AM, DiFazio R, Flynn JL. IFN-γ from CD4 T cells is essential for host survival and enhances CD8 T cell function during Mycobacterium tuberculosis infection. Journal of immunology (Baltimore, Md : 1950). 2013;190(1):270-.

57. Sørensen M, Munk OL, Mortensen FV, Olsen AK, Bender D, Bass L, Keiding S. Hepatic uptake and metabolism of galactose can be quantified in vivo by 2-[18F]fluoro-2-deoxygalactose positron emission tomography. American Journal of Physiology Gastrointestinal and Liver Physiology. 2008;295(1):G27-G.
58. Meireles P, Sales-Dias J, Andrade CM, Mello-Vieira J, Mancio-Silva L, Simas JP, et al. GLUT1-mediated glucose uptake plays a crucial role during Plasmodium hepatic infection. Cellular Microbiology. 2017;19(2):e12646-e.
59. Azman KF, Safdar A, Zakaria R. D-galactose-induced liver aging model: Its underlying mechanisms and potential therapeutic interventions. Experimental Gerontology. 2021;150:111372-.
60. Zatorski H, Salaga M, Zielińska M, Mokrowiecka A, Jacenik D, Krajewska WM, et al. Colonic inflammation induces changes in glucose levels through modulation of incretin system. Pharmacological Reports. 2021;73(6):1670-9.
61. Boström PJ, Thoms J, Sykes J, Ahmed O, Evans A, Rhijn BWGV, et al. Hypoxia Marker GLUT-1 (Glucose Transporter 1) is an Independent Prognostic Factor for Survival in Bladder Cancer Patients Treated with Radical Cystectomy. Bladder Cancer. 2016;2(1):101-.
62. Rengachar P, Bhatt AN, Polavarapu S, Veeramani S, Krishnan A, Sadananda M, Das UN. Gamma-Linolenic Acid (GLA) Protects against Ionizing Radiation-Induced Damage: An In Vitro and In Vivo Study. Biomolecules 2022, Vol 12, Page 797. 2022;12(6):797-.
63. Lee TC, Ivester P, Hester AG, Sergeant S, Case LD, Morgan T, et al. The impact of polyunsaturated fatty acid-based dietary supplements on disease biomarkers in a metabolic syndrome/diabetes population. Lipids in Health and Disease. 2014;13(1):1-11.
64. Sergeant S, Rahbar E, Chilton FH. Gamma-linolenic acid, Dihommo-gamma linolenic, Eicosanoids and Inflammatory Processes. European journal of pharmacology. 2016;785:77-.
65. Barham JB, Edens MB, Fonteh AN, Johnson MM, Easter L, Chilton FH. Addition of eicosapentaenoic acid to gamma-linolenic acid-supplemented diets prevents serum arachidonic acid accumulation in humans. The Journal of nutrition. 2000;130(8):1925-31.
66. Queck A, Thomas D, Jansen C, Schreiber Y, Rüschenbaum S, Praktiknjo M, et al. Pathophysiological role of prostanoids in coagulation of the portal venous system in liver cirrhosis. PLOS ONE. 2019;14(10):e0222840-e.
67. Milosevic I, Vujovic A, Barac A, Djelic M, Korac M, Spurnic AR, et al. Gut-Liver Axis, Gut Microbiota, and Its Modulation in the Management of Liver Diseases: A Review of the Literature. International Journal of Molecular Sciences 2019, Vol 20, Page 395. 2019;20(2):395-.
68. Salviati L, Trevisson E, Doimo M, Navas P. Primary Coenzyme Q10 Deficiency. GeneReviews®. 2017.

69. Mantle D, Lopez-Lluch G, Hargreaves IP. Coenzyme Q10 Metabolism: A Review of Unresolved Issues. International Journal of Molecular Sciences 2023, Vol 24, Page 2585. 2023;24(3):2585-.

70. Dragan S, Buleu F, Christodorescu R, Cobzariu F, Iurciuc S, Velimirovici D, et al. Benefits of multiple micronutrient supplementation in heart failure: A comprehensive review. https://doiorg/101080/1040839820181540398. 2018;59(6):965-81.

71. Olivieri F, Lazzarini R, Babini L, Prattichizzo F, Rippo MR, Tiano L, et al. Anti-inflammatory effect of ubiquinol-10 on young and senescent endothelial cells via miR-146a modulation. Free Radical Biology and Medicine. 2013;63:410-20.

72. Farsi F, Ebrahimi-Daryani N, Barati M, Janani L, Karimi MY, Akbari A, et al. Effects of coenzyme Q10 on health-related quality of life, clinical disease activity and blood pressure in patients with mild to moderate ulcerative colitis: a randomized clinical trial. Medical Journal of the Islamic Republic of Iran. 2021;35(1):3-.

73. Moura FA, de Andrade KQ, dos Santos JCF, Araújo ORP, Goulart MOF. Antioxidant therapy for treatment of inflammatory bowel disease: Does it work? Redox Biology. 2015;6:617-39.

74. Cinelli MA, Lee KSS. Asymmetric Total Synthesis of 19,20-Epoxydocosapentaenoic Acid, a Bioactive Metabolite of Docosahexaenoic Acid. Journal of Organic Chemistry. 2019;84(23):15362-72.

75. Capozzi ME, Penn JS. Epoxydocosapentaenoic acid (EDP) and epoxyeicosatrienoic acid (EET) affect TNFα production and leukocyte adhesion in diabetic retinopathy. Investigative Ophthalmology & Visual Science. 2016;57(12).

76. Molfino A, Amabile MI, Lionetto L, Spagnoli A, Ramaccini C, Luca AD, et al. DHA Oral Supplementation Modulates Serum Epoxydocosapentaenoic Acid (EDP) Levels in Breast Cancer Patients. Oxidative medicine and cellular longevity. 2019;2019.

77. Dalli J, Colas RA, Quintana C, Barragan-Bradford D, Hurwitz S, Levy BD, et al. Human Sepsis Eicosanoid and Proresolving Lipid Mediator Temporal Profiles: Correlations with Survival and Clinical Outcomes. Critical Care Medicine. 2017;45(1):58-68.

78. Zhang G, Panigrahy D, Mahakian LM, Yang J, Liu JY, Lee KSS, et al. Epoxy metabolites of docosahexaenoic acid (DHA) inhibit angiogenesis, tumor growth, and metastasis. Proceedings of the National Academy of Sciences of the United States of America. 2013;110(16):6530-5.

Figures and Legends:

Figures:

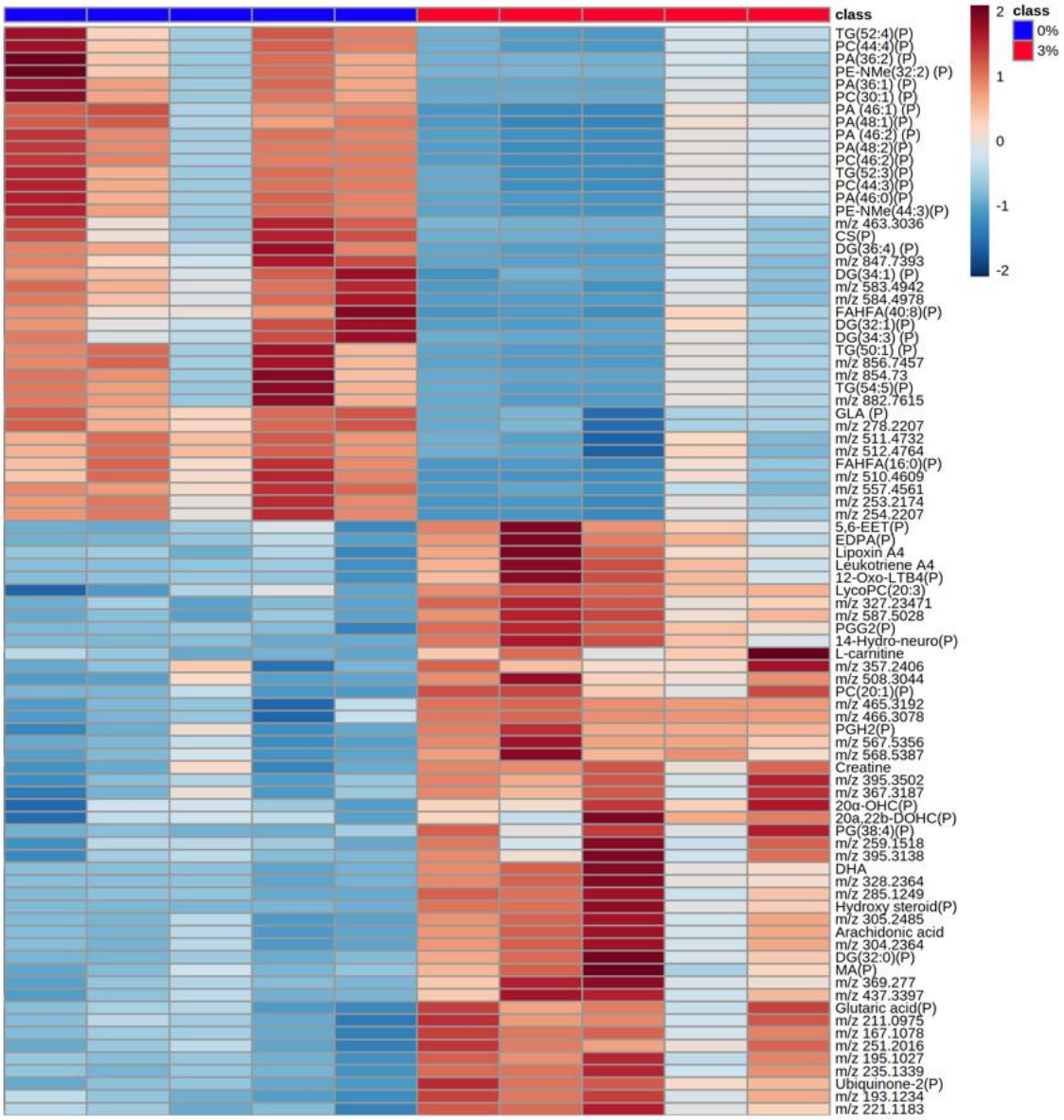

Figure 1A. Heatmap of metabolites increased and decreased in abundance in the ileum of 3% DSS treated mice compared to controls. Heatmap shows *m/z* of molecules unable to be identified, putatively identified molecules (marked with a P) and molecules with an MSMS confirmed identification. Heatmap was created using Metaboanalyst 5.0. The colour of each sample is proportional to the significance of change in metabolite abundance indicated by the colour bar (red, up-regulated in DSS colitis group; blue, down-regulated in colitis group). Rows correspond to metabolites and columns correspond to samples.

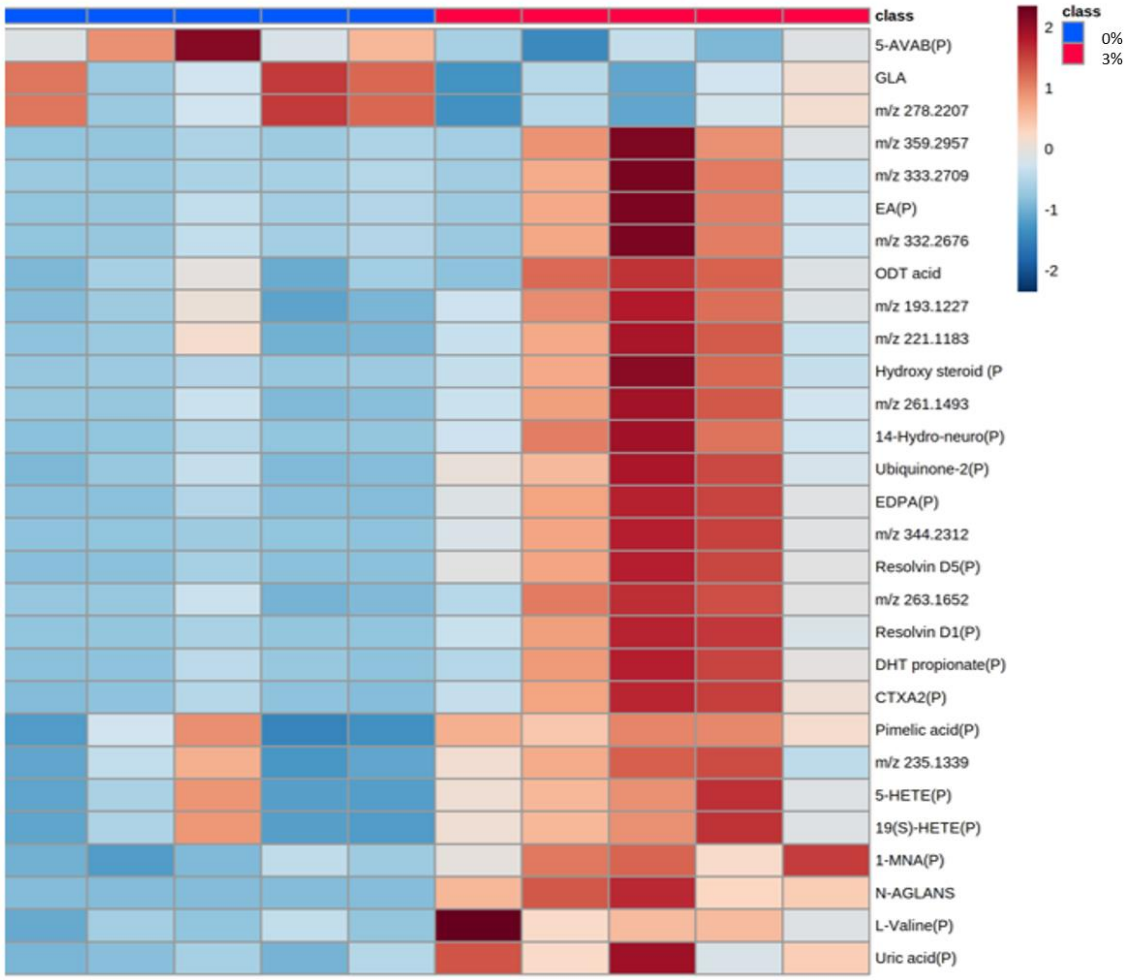

Figure 1B. Heatmap of metabolites increased and decreased in abundance in the colon of 3% DSS treated mice compared to controls. Heatmap shows *m/z* of molecules unable to be identified, putatively identified molecules (marked with a P) and molecules with an MSMS confirmed identification. Heatmap was created using Metaboanalyst 5.0. The colour of each sample is proportional to the significance of change in metabolite abundance indicated by the colour bar (red, up-regulated in DSS colitis group; blue, down-regulated in colitis group). Rows correspond to metabolites and columns correspond to samples.

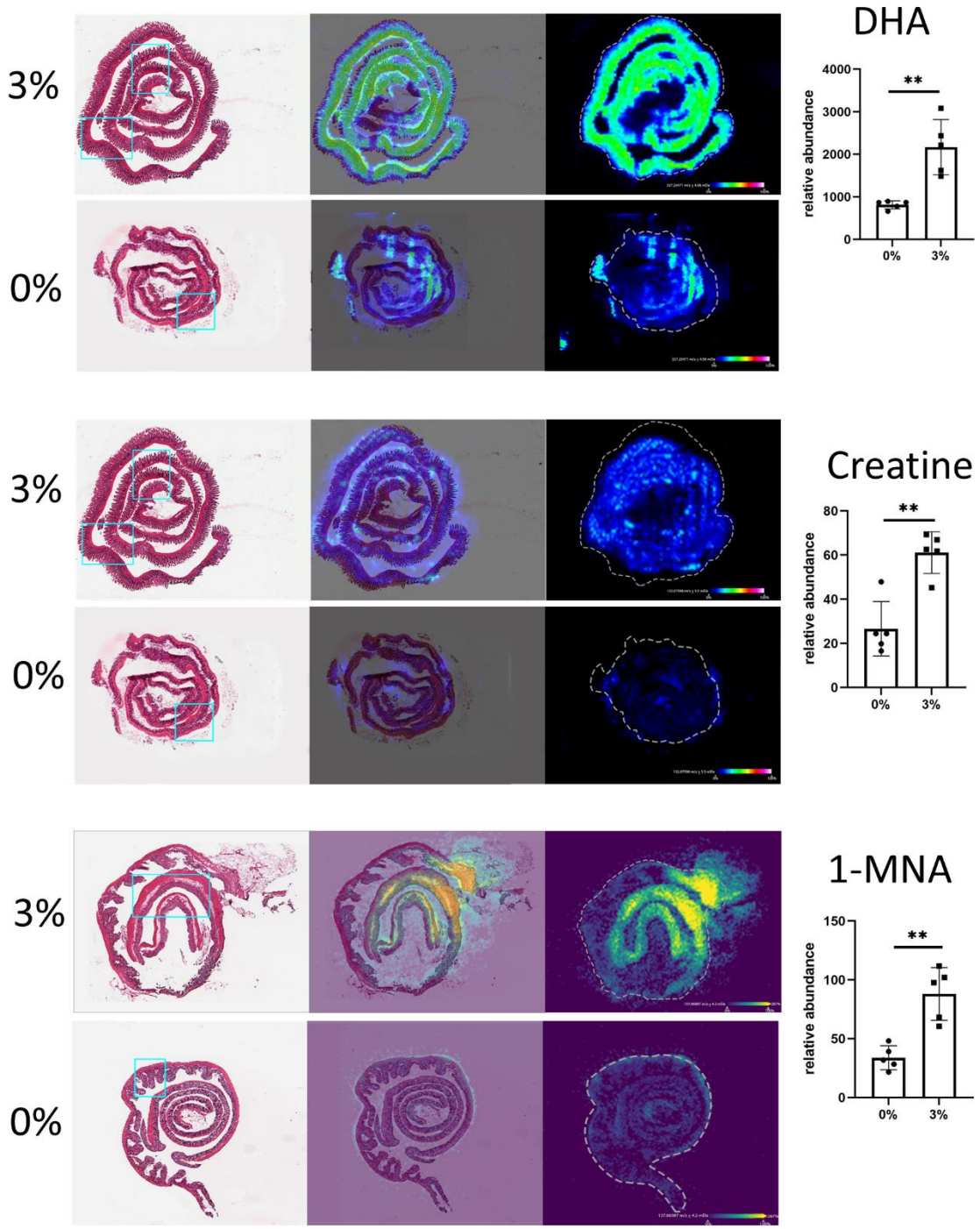

Figure 2. MSI of DHA, Creatine and 1-MNA abundance in the intestine. From left to right; haematoxylin and eosin (H&E)-stained sections, overlayed image of H&E image and MSI of specific molecule, MSI heatmap of molecules (colour bar shows 0% to 100% relative abundance). Bar plot shows the relative abundance of DHA and Creatine in the ileum and 1-MNA in the colon. Data are shown as the mean of five biological replicates ± standard

deviation (SD) (error bars). Multiple T-test was performed with FDR 5% adjustment to compare metabolite abundance between the groups (0% DSS and 3% DSS) *$p<0.05$, **$p<0.01$, ***$p<0.001$, ****$p<0.0001$ was considered statistically significant. Blue rectangular box shows the tissue region selected for IMC.

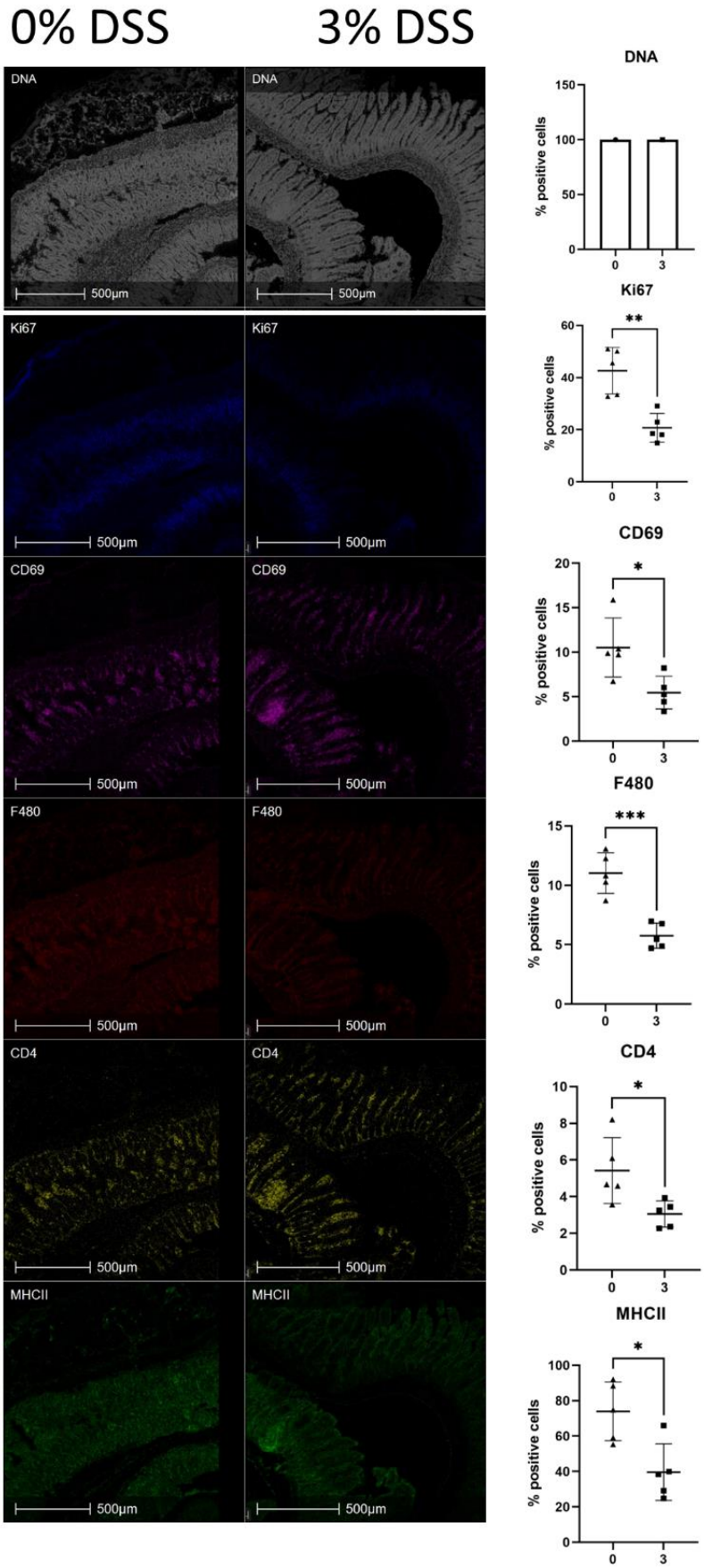

1067

Figure 3. Representative IMC images of biological markers of cell function in the ileum of DSS colitis model. Image shown is the region indicated in Fig 2. From top to bottom, DNA intercalator identified single cells within the tissue section, markers for cell proliferation and immune cell function are shown (fold change and *p* value); Ki67 (2.05-fold, *p*=0.0016), CD69 (1.96-fold, *p*=0.0176), F480 (2.0-fold, *p*=0.0004), CD4 (1.77-fold, *p*=0.0252) and MHCII (1.86-fold, *p*=0.0105). Percentage positive cells represented as bar graph showing five biological replicates. T-test performed to compare the two groups and **p*<0.05, ***p*<0.01, ****p*<0.001, *****p*<0.0001 was considered statistically significant.

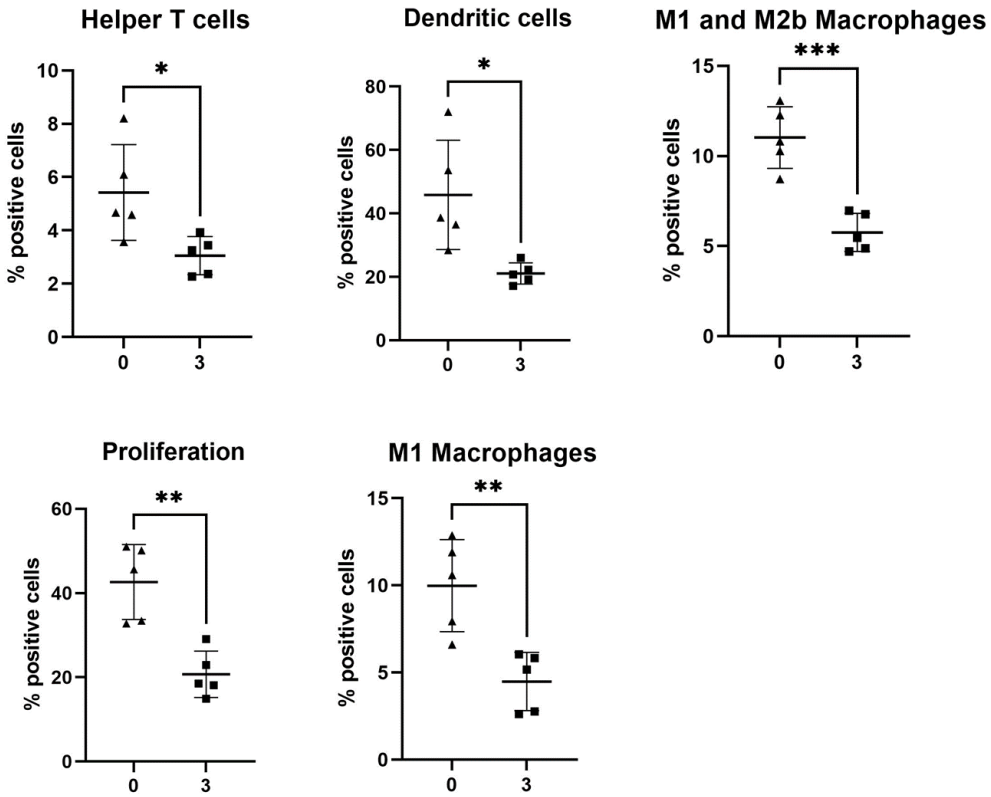

Figure 4. Cell phenotype and function are significantly changed in the ileal mucosa of DSS-treated mice. Percentage positive cells represented as bar graph showing five biological replicates. Helper T cells ($CD3^+$, $CD4^+$)(1.78-fold, *p*=0.0252), dendritic cells ($CD11c^+$, $MHCII^+$)(2.17-fold, *p*=0.0136), M2b (1.91-fold, *p*=0.0004) and M1 macrophages ($F480^+$)(2.22-fold, *p*=0.0043), and proliferation positive cells ($Ki67^+$)(2.05-fold, *p*=0.0016) were decreased in the 3% DSS treated colitis group compared to the control. T-test performed to compare the two groups and **p*<0.05, ***p*<0.01, ****p*<0.001, *****p*<0.0001 was considered statistically significant.

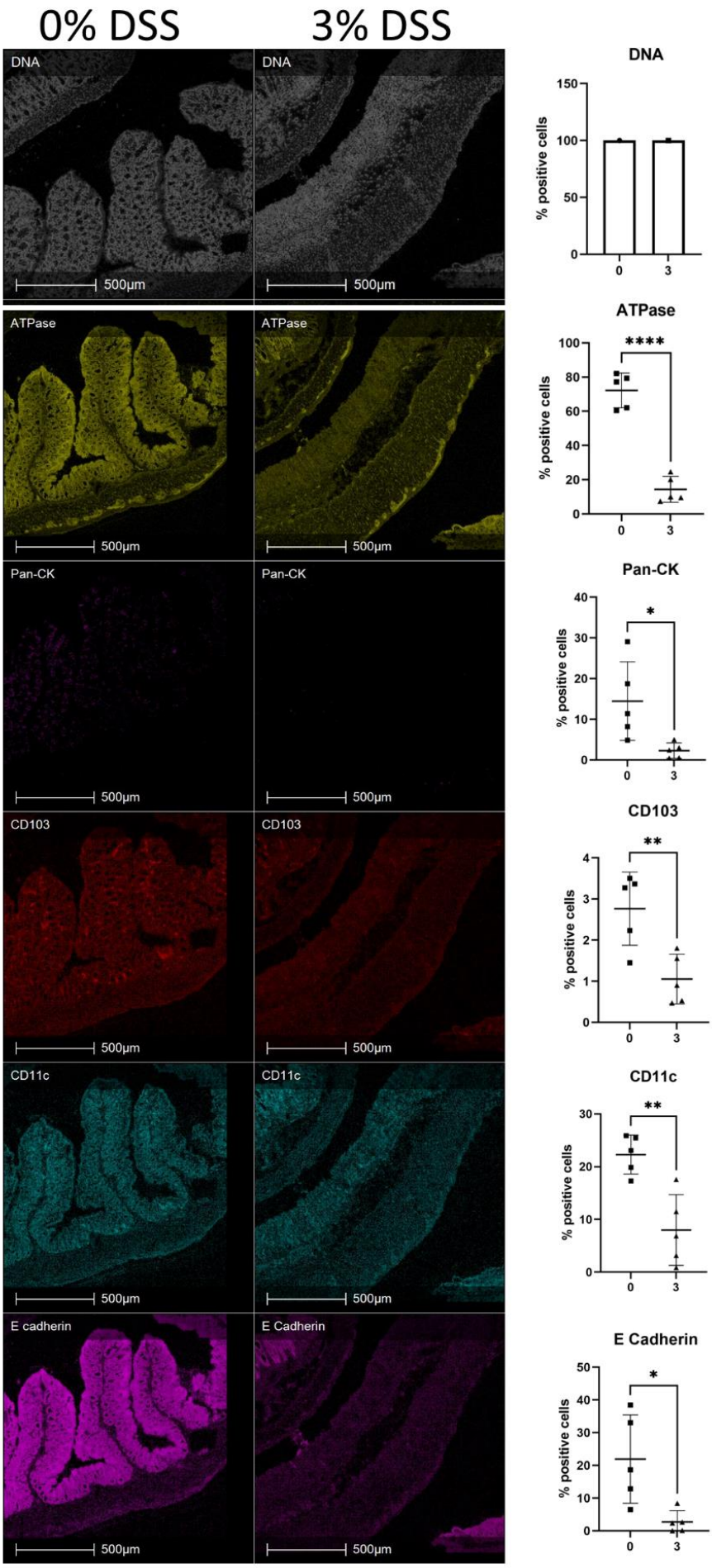
0% DSS
3% DSS
DNA
ATPase
Pan-CK
CD103
CD11c
E cadherin
E Cadherin
500µm
% positive cells
****
*
**

1088

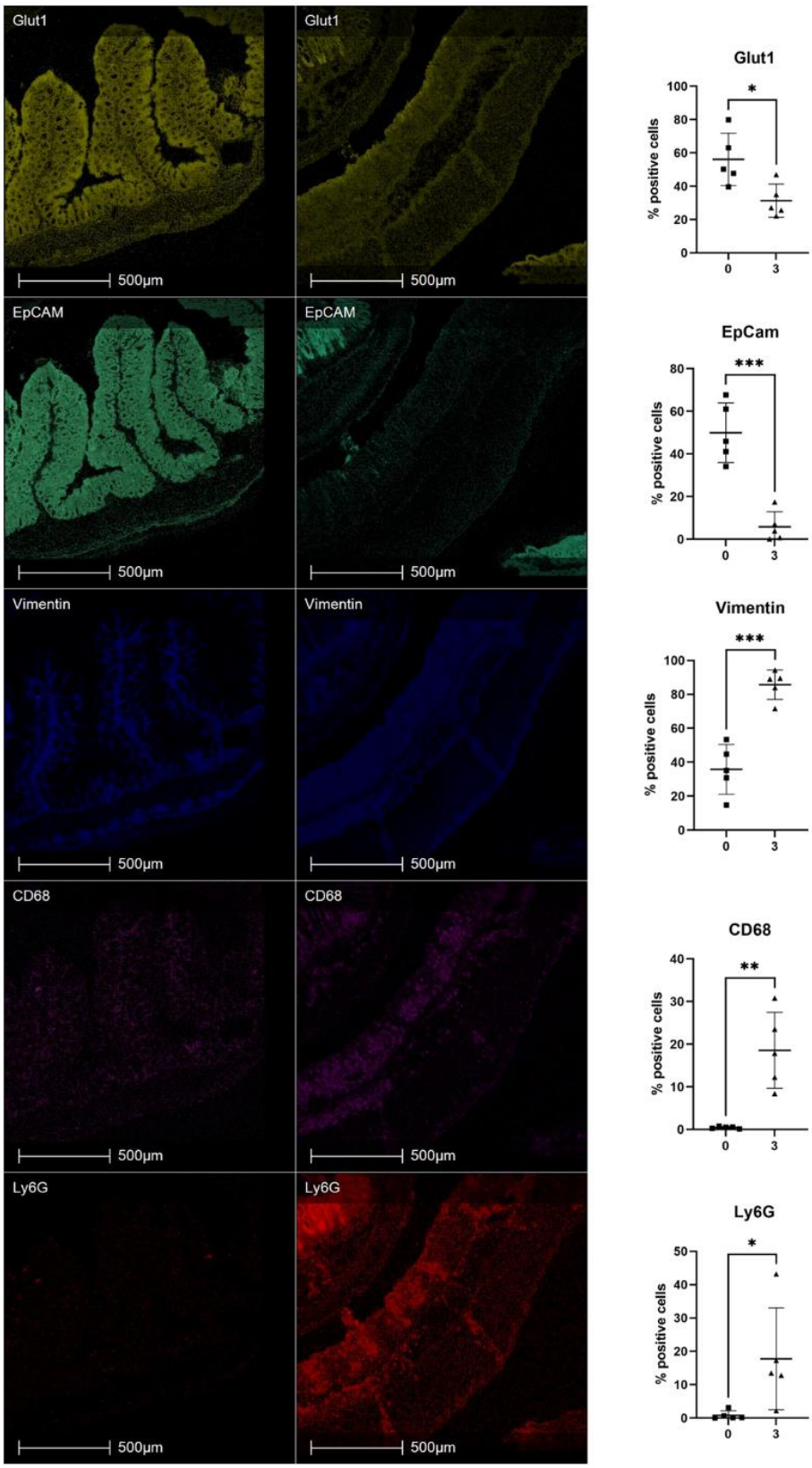
Glut1
500µm
EpCAM
Vimentin
CD68
Ly6G
Glut1
% positive cells
*
EpCam
***
Vimentin
CD68
**
Ly6G
0
3

1089

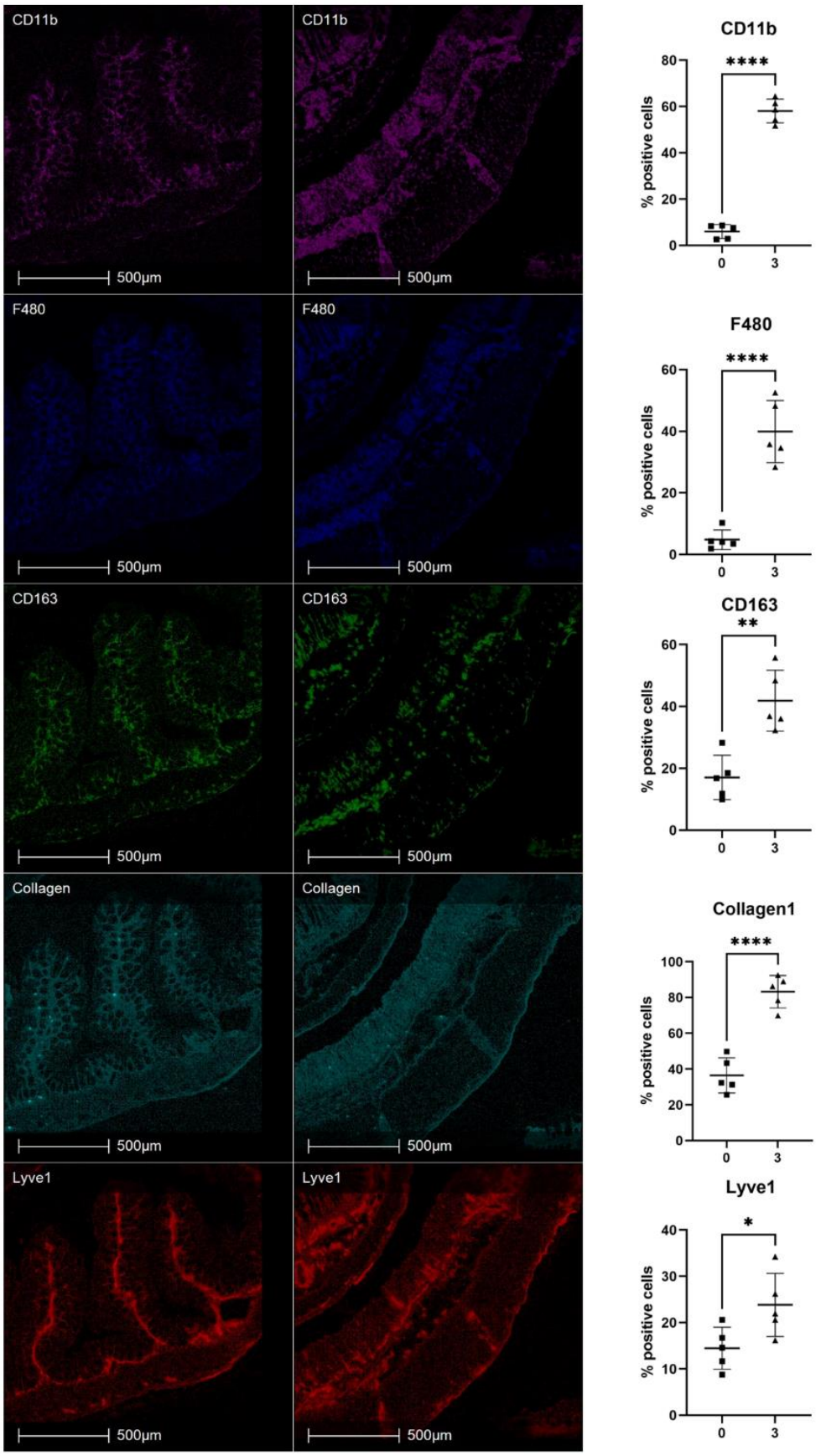
CD11b
CD11b
500µm
500µm
CD11b
****
% positive cells
80
60
40
20
0
0
3
F480
F480
500µm
500µm
F480
****
% positive cells
60
40
20
0
0
3
CD163
CD163
500µm
500µm
CD163
**
% positive cells
60
40
20
0
0
3
Collagen
Collagen
500µm
500µm
Collagen1
****
% positive cells
100
80
60
40
20
0
0
3
Lyve1
Lyve1
500µm
500µm
Lyve1
*
% positive cells
40
30
20
10
0
0
3

1090

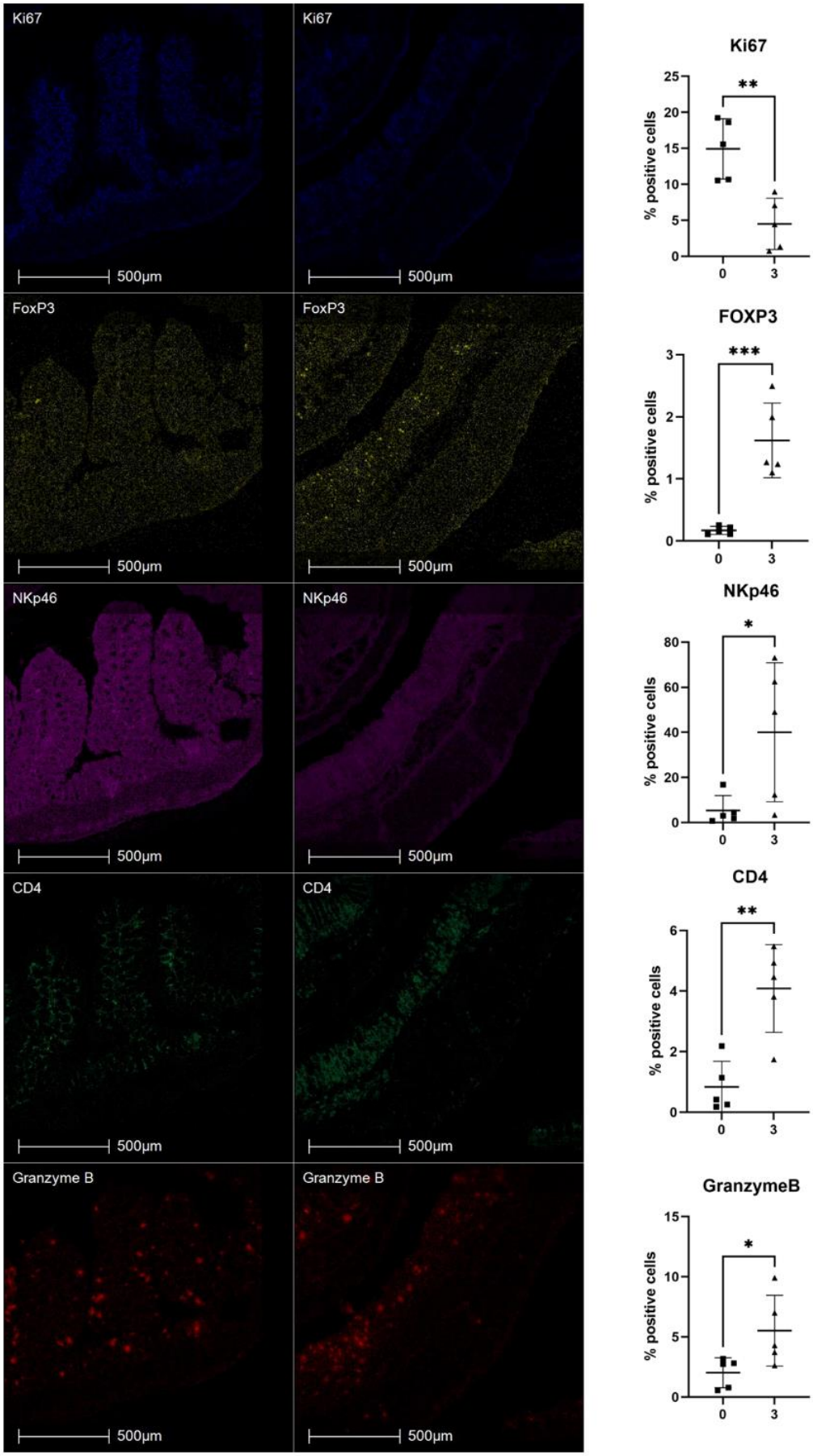
Ki67
Ki67
500µm
500µm
FoxP3
FoxP3
500µm
500µm
NKp46
NKp46
500µm
500µm
CD4
CD4
500µm
500µm
Granzyme B
Granzyme B
500µm
500µm
Ki67
**
% positive cells
0
5
10
15
20
25
0
3
FOXP3
***
% positive cells
0
1
2
3
0
3
NKp46
*
% positive cells
0
20
40
60
80
0
3
CD4
**
% positive cells
0
2
4
6
0
3
GranzymeB
*
% positive cells
0
5
10
15
0
3

1091

Figure 5. Representative IMC images of biological markers of cell function in the colon of DSS colitis model. Image shown is the same region as in Fig. 2. From top to bottom, DNA intercalator identified single cells within the tissue section, markers for cell proliferation and immune cell function ATPase, Pan-CK, CD103, CD11c, E Cadherin, Glut1, EpCAM, Vimentin, CD68, Ly6G, CD11b, F480, CD163, Collagen1, Lyve1, Ki67, FOXP3, NKp46, CD4 and Granzyme B. Percentage positive cells represented as bar graph showing five biological replicates. T-test performed to compare the two groups and *$p<0.05$, **$p<0.01$, ***$p<0.001$, ****$p<0.0001$ was considered statistically significant. Markers that decreased included ATPase 5.01-fold ($p<0.0001$), Pan-CK 6.24-fold ($p=0.0246$), CD103 2.62-fold ($p=0.0074$), CD11c 2.62-fold ($p=0.0074$), E Cadherin 2.79-fold ($p=0.0030$), Glut1 1.78-fold ($p=0.0177$), Ki67 3.3-fold ($p=0.0028$) and EpCAM 3.30-fold ($p=0.0028$). In contrast the following markers increased significantly post-DSS treatment; vimentin 2.39-fold ($p=0.0002$), CD68 39.18-fold ($p=0.0019$), Ly6G 22.13-fold ($p=0.0382$), CD11b 9.64-fold ($p<0.0001$), F480 8.30-fold ($p<0.0001$), CD163 2.45-fold ($p=0.0018$), collagen 2.28-fold ($p<0.0001$), Lyve1 1.64-fold ($p=0.0342$), FoxP3 9.50-fold ($p=0.0007$), NKp46 7.42-fold ($p=0.0393$), CD4 4.88-fold ($p=0.0025$), and granzyme B 2.72-fold ($p=0.0402$).

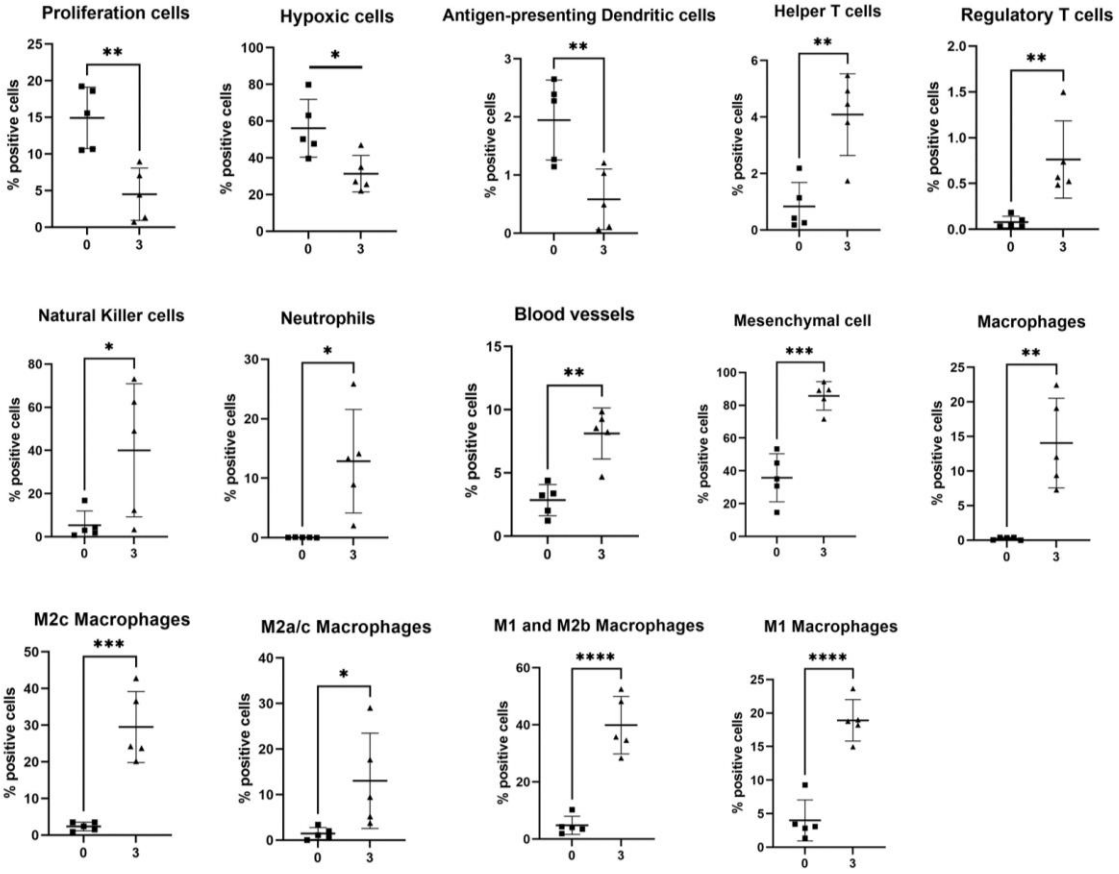

Figure 6. Bar graph of cell phenotype and function significantly changed in the colonic mucosa. Percentage positive cells represented as bar graph showing five biological replicates. Proliferative (Ki67$^+$), hypoxic (Glut1$^+$), and antigen-presenting dendritic cells (CD11c$^+$, MHCII$^+$, CD103$^+$) were reduced and Helper T cells (CD3$^+$, CD4$^+$), regulatory T cells (CD3$^+$, CD4$^+$, FOXP3$^+$), natural killer (NK) cells (NKp46$^+$), Neutrophils (Ly6G$^+$, CD11b$^+$), blood vessels (CD31$^+$), mesenchymal cells (vimentin$^+$), macrophages (F480$^+$, CD68$^+$, CD11b$^+$) and macrophage subsets including M2c (F480$^+$, CD163$^+$), M2a(F480$^+$, CD206$^+$), M2b (F480$^+$) and M1 (F480$^+$, MHCII$^+$) were increased in the 3% group compared to the control. T-test performed to compare the two groups and *p<0.05, **p<0.01, ***p<0.001, ****p<0.0001 was considered statistically significant.

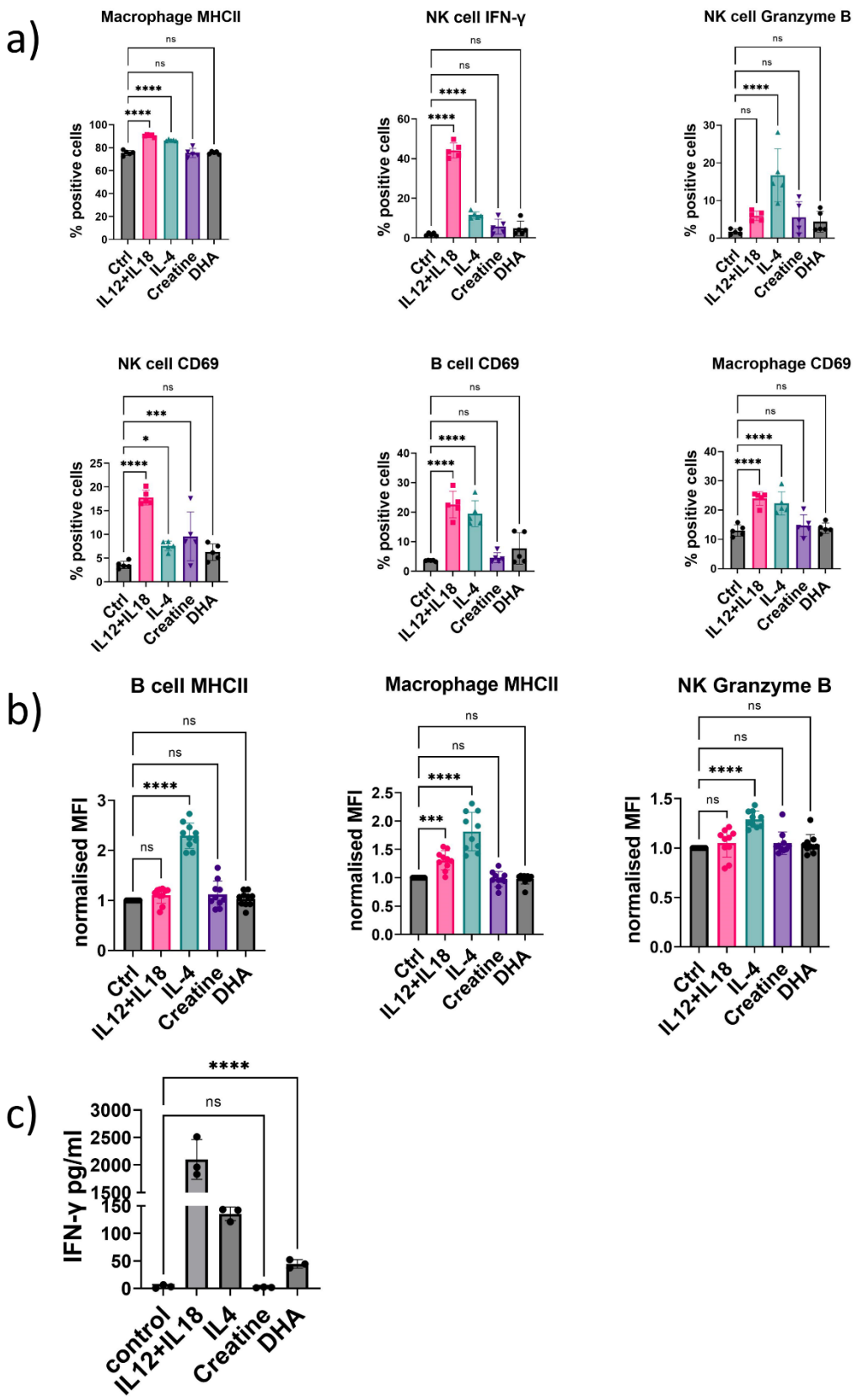

Figure 7. Flow cytometry and cytokine release analysis of splenic immune cells following stimulation with creatine and DHA. Immune cells were isolated from spleen tissue and stimulated with 50 µM creatine or DHA as well as IL12+IL-18 and IL4 as positive

immune activating controls. A) Percentage of immune cells (NK cells, B cells and macrophages) positively expressing specific markers (MHCII, IFN-γ, Granzyme B and CD69). B) Mean fluorescence intensity (MFI) was normalised to control (no stimulation) and shows the relative amount of expressed marker within a positive population. A-B) One-way ANOVA was performed to compare stimulation versus the control condition (cells without treatment). C) ELISA was used to quantify the release of IFN-γ into immune cell supernatant and is shown as pg/ml. Unpaired T-test was performed to compared creatine or DHA stimulated groups to control and did not include positive controls (cytokine stimulations). Data is shown as the mean of 3 biological replicates ± standard deviation (SD). *$p<0.05$, **$p<0.01$, ***$p<0.001$, ****$p<0.0001$ is considered statistically significant.

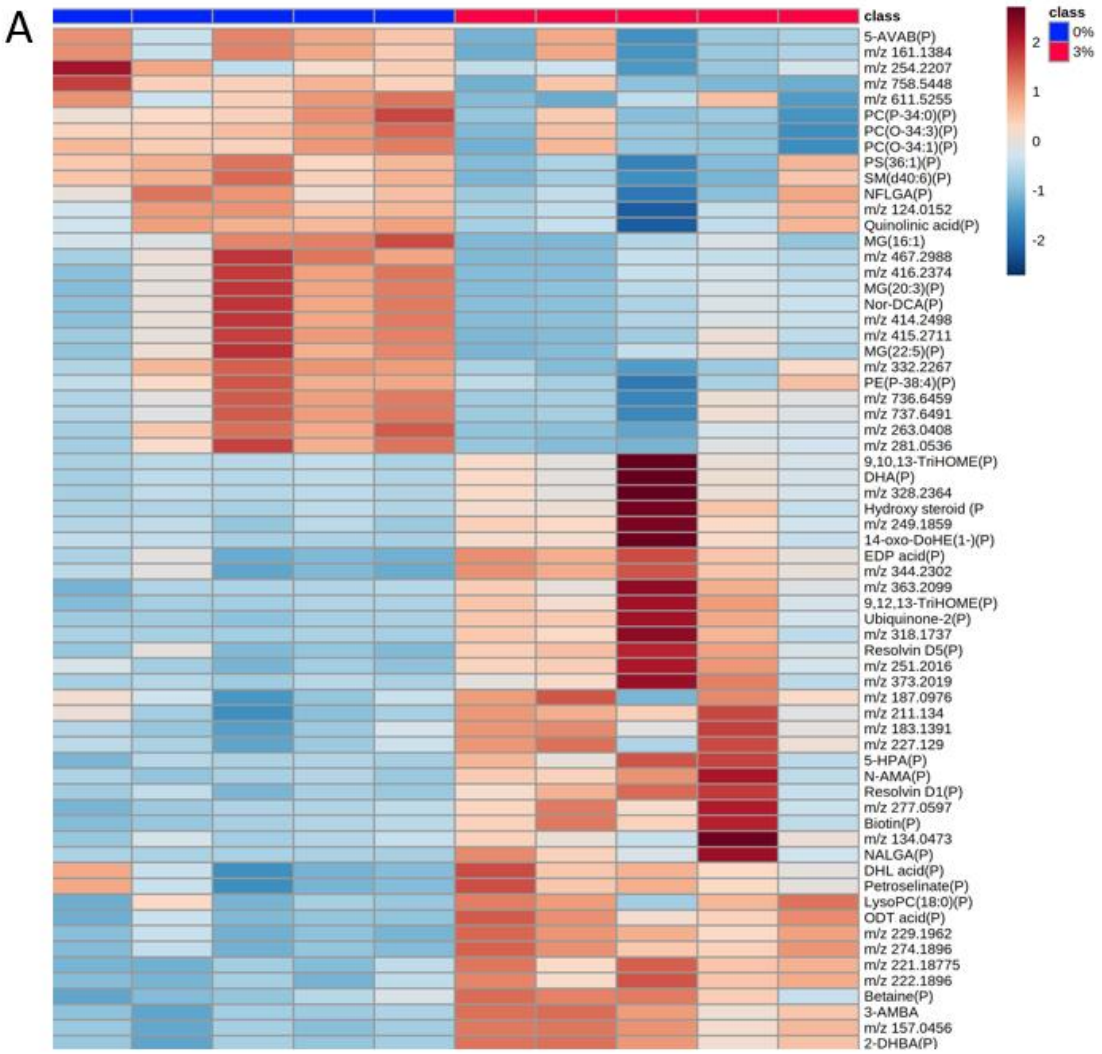

Figure 8. Heatmap of metabolites increased and decreased in abundance in the spleen of 3% DSS treated mice compared to controls. Heatmap shows *m/z* of unidentified molecules, putatively identified molecules (marked with a P). Heatmap was created using Metaboanalyst 5.0. The colour of each sample is proportional to the significance of change in metabolite abundance indicated by the colour bar (red, up-regulated in DSS colitis group; blue, down-regulated in colitis group). Rows correspond to metabolites and columns correspond to samples.

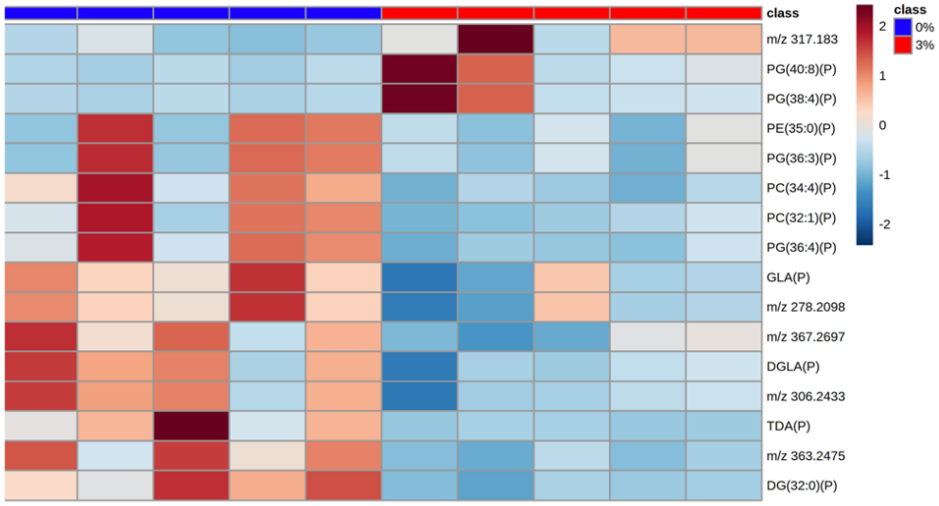

Figure 9. Heatmap of metabolites increased and decreased in abundance in the kidney of 3% DSS treated mice compared to controls. A) Heatmap shows *m/z* of molecules unable to be identified, putatively identified molecules (marked with a P). Heatmap was created using Metaboanalyst 5.0. The colour of each sample is proportional to the significance of change in metabolite abundance indicated by the colour bar (red, up-regulated in DSS colitis group; blue, down-regulated in colitis group). Rows correspond to metabolites and columns correspond to samples.

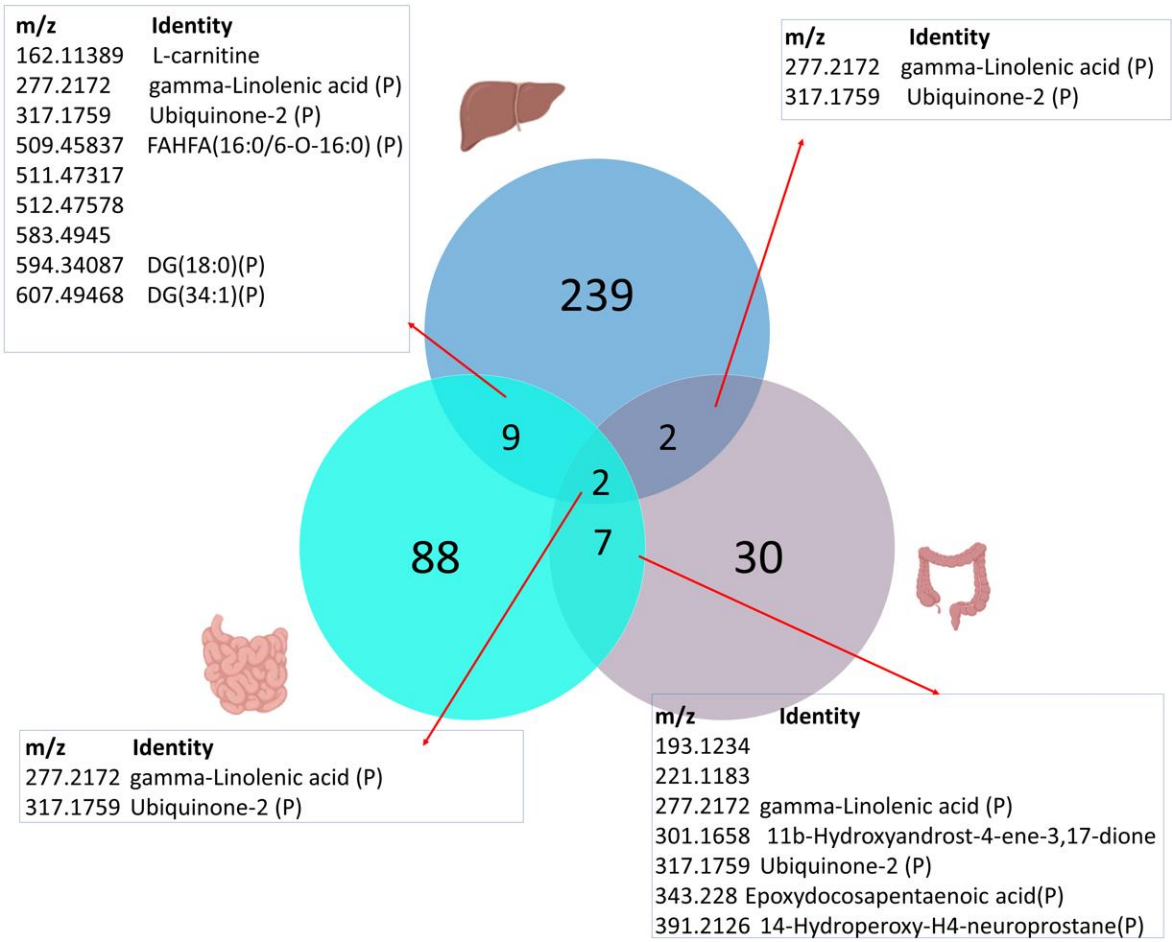

Figure 10. Venn diagram showing molecules altered in the ileum, colon, and liver in 3% DSS treated mice compared to controls. The top circle represents the 239 molecular changes in the liver, bottom-left circle represents 88 molecular changes in ileum and bottom-right represents 30 molecular changes in the colon. Overlapped segments indicate the number of molecules that are changed similarly between different tissue. The *m/z* and putative identities of the molecules commonly shared between tissue are highlighted in boxes.

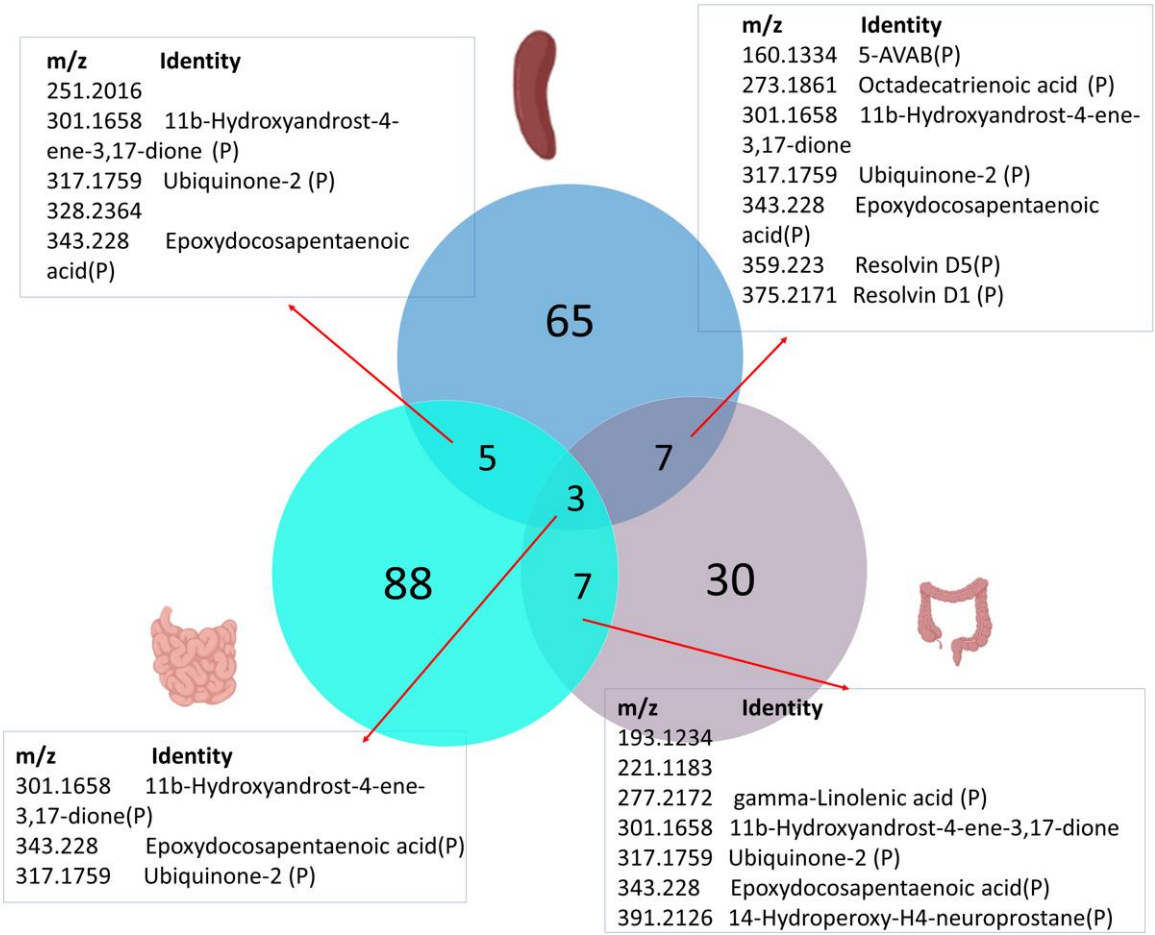

Figure 11. Venn diagram of molecules altered in the ileum, colon, and spleen in 3% DSS treated mice compared to controls. The top circle represents the 65 molecular changes in the liver, bottom-left circle represents 88 molecular changes in ileum and bottom-right represents 30 molecular changes in the colon. Overlapped segments indicate the number of molecules that are changed similarly between different tissue. The *m/z* and putative identities of the molecules commonly shared between tissue are highlighted in boxes.

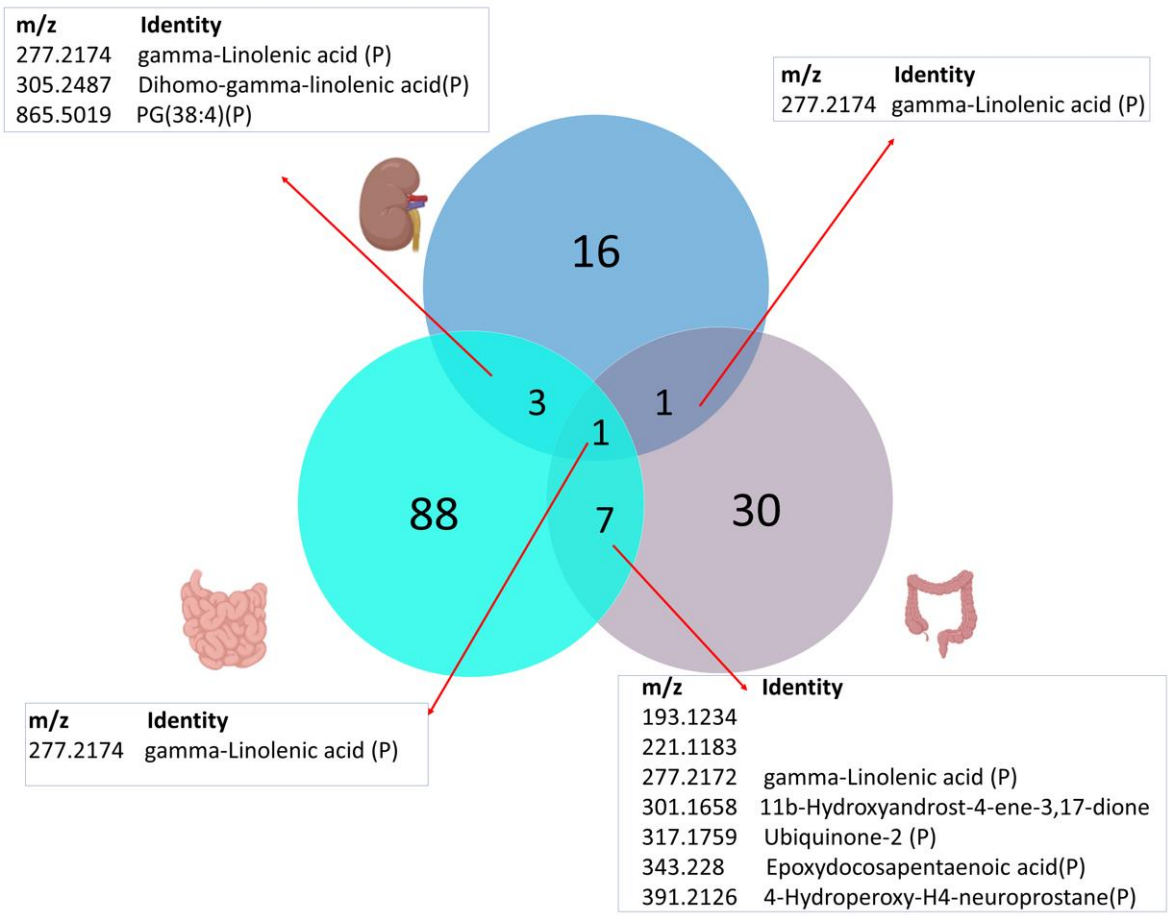

Figure 12. Venn diagram of molecules altered in the ileum, colon, and kidney in 3% DSS treated mice compared to controls. The top circle represents the 16 molecular changes in the kidney, bottom-left circle represents 88 molecular changes in ileum and bottom-right represents 30 molecular changes in the colon. Overlapped segments indicate the number of molecules that are changed similarly between different tissue. The *m/z* and putative identities of the molecules commonly shared between tissue are highlighted in boxes.

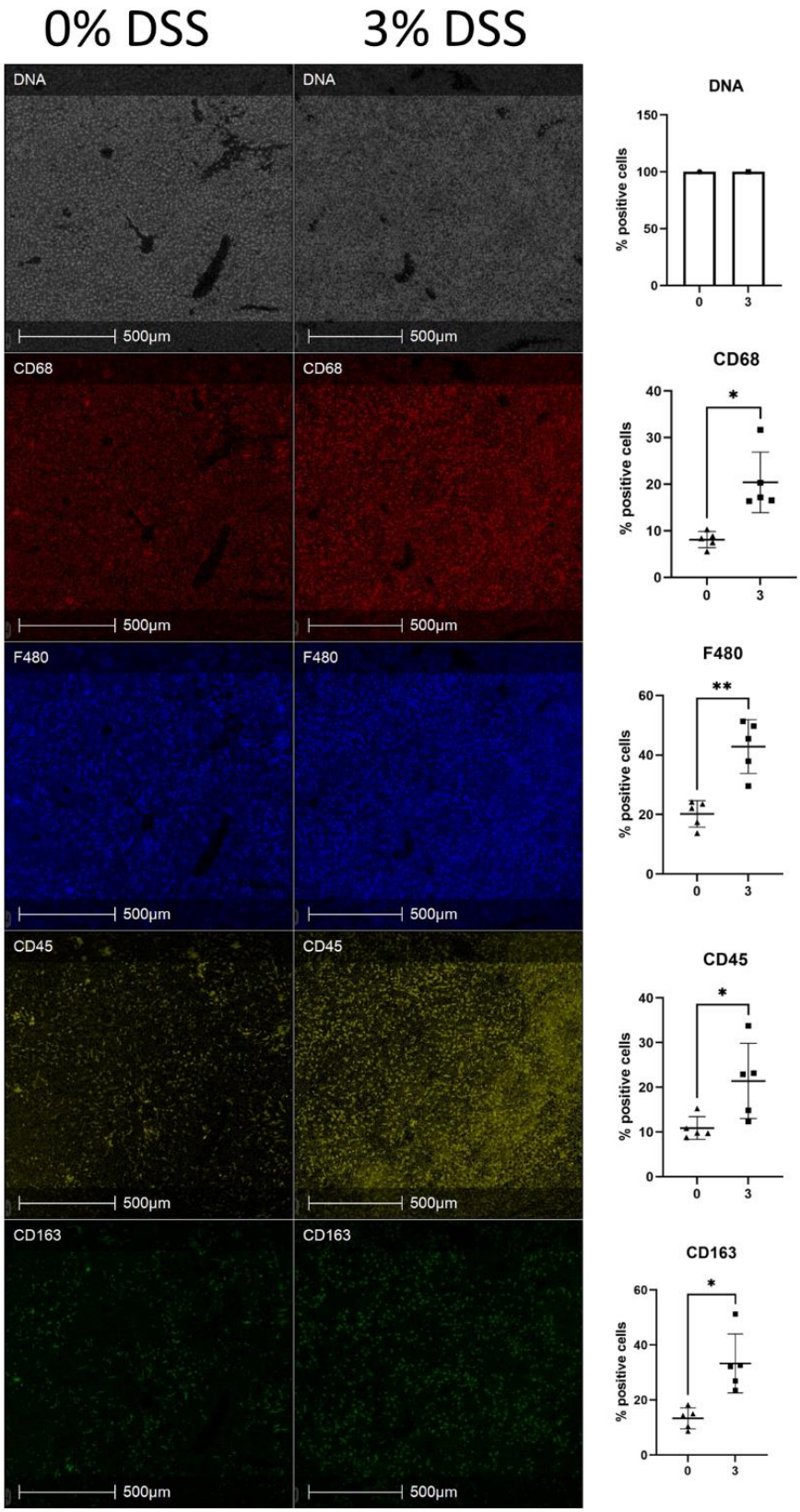
0% DSS
3% DSS
DNA
DNA
500µm
500µm
CD68
CD68
500µm
500µm
F480
F480
500µm
500µm
CD45
CD45
500µm
500µm
CD163
CD163
500µm
500µm
DNA
% positive cells
150
100
50
0
0
3
CD68
*
% positive cells
40
30
20
10
0
0
3
F480
**
% positive cells
60
40
20
0
0
3
CD45
*
% positive cells
40
30
20
10
0
0
3
CD163
*
% positive cells
60
40
20
0
0
3

1215

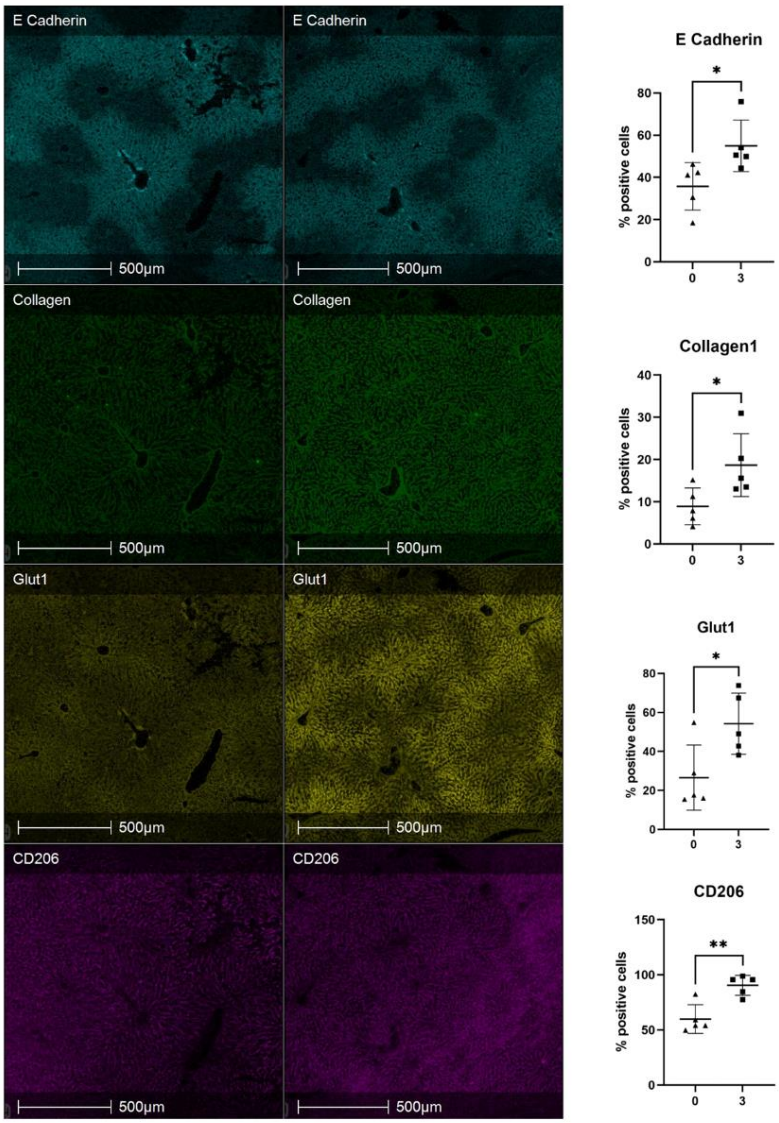

Figure 13. Representative IMC images of biological markers of cell function in the liver of 3% DSS treated and control untreated mice. From top to bottom, DNA intercalator identified single cells within the tissue section, markers for cell proliferation and immune cell function CD68, F480, CD45, CD163, E Cadherin, Collagen1, Glut1 and CD206. Percentage positive cells represented as bar graph showing five biological replicates. T-test performed to compare the two groups and **p*<0.05, ***p*<0.01, ****p*<0.001, *****p*<0.0001 was considered statistically significant. The percentage of cells expressing markers $CD68^+$ (2.50-fold, *p*=0.0114), $CD45^+$ (1.96-fold, *p*=0.0465), $F480^+$ (2.11-fold, *p*=0.0026), $CD163^+$ (2.49-fold, *p*=0.0113), E $cadherin^+$ (1.53-fold, *p*=0.00325), $collagen^+$ (2.09-fold, *p*=0.0422), $Glut1^+$ (2.03-fold, *p*=0.0272) and $CD206^+$ (1.50-fold, *p*=0.0033) all showed an increase.

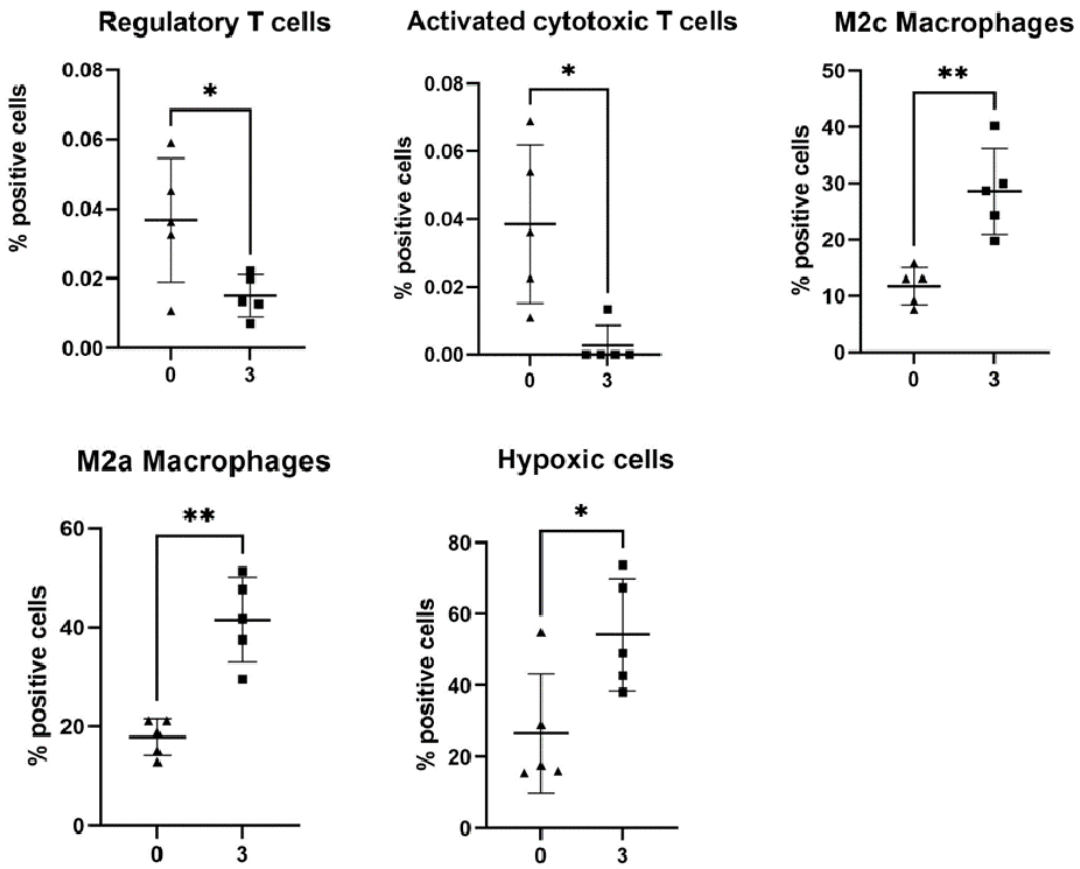

Figure 14. Bar graphs denoting significant changes in cell phenotype and function in the liver in 3% DSS treated mice. Percentage positive cells represented as bar graph showing five biological replicates and Regulatory T cells ($CD3^+$, $CD4^+$, $FOXP3^+$) and Activated cytotoxic T cells ($CD3^+$, $CD8^+$, Granzyme B^+) significantly reduced; whereas, the percentage of macrophages in the subclass M2c ($F480^+$, $CD163^+$) and M2a ($F480^+$, $CD206^+$) and hypoxia ($Glut1^+$) were significantly upregulated in 3% group compared to the control. T-test performed to compare the two groups and *p<0.05, **p<0.01, ***p<0.001, ****p<0.0001 was considered statistically significant.